



Strengthening of pretreated aluminum during ultrasonic additive manufacturing[☆]

Michael Pagan^{a,*}, Ningxiner Zhao^b, Leon M. Headings^b, Marcelo J. Dapino^b, Sriram Vijayan^b, Joerg R. Jinschek^{b,c}, Steven J. Zinkle^{a,d}, S.S. Babu^{a,d}

^a University of Tennessee, Knoxville, TN 37916, United States

^b The Ohio State University, Columbus, OH 43210, United States

^c National Centre for Nano Fabrication & Characterisation, Technical University of Denmark, Kgs. Lyngby, Denmark

^d Oak Ridge National Laboratory, Oak Ridge, TN 37831, United States

ARTICLE INFO

Keywords:

Ultrasonic additive manufacturing
Mechanical properties
Aluminum alloys
Microstructure evolution
Lattice defect formation

ABSTRACT

Strengthening effects in materials bonded by the high strain rate plastic deformation process, Ultrasonic Additive Manufacturing (UAM), were investigated. Aluminum (Al 6061) was pretreated by tempering and annealing prior to bonding through UAM. Following UAM, multiscale material characterization was performed. Tensile testing in the rolling (x) direction demonstrated the material became harder after the UAM process, and nanoindentation demonstrated the foil-foil interfaces became harder than the bulk foil material. The strengthening effects are a result of microstructure changes at the interfaces and in the bulk foil regions which were characterized using X-ray diffraction, scanning electron microscopy, transmission electron microscopy, and energy dispersive spectroscopy. These microstructure changes result from dynamic recrystallization, dynamic recovery, adiabatic heating, and precipitate dissolution. This study signifies the metallurgical features creating mechanical strength increases, rather than decreases, in UAM builds.

1. Introduction

Ultrasonic additive manufacturing (UAM) is a solid-state additive manufacturing bonding process that relies on ultrasonic welding to join thin foils (~150 μm) at relatively low temperatures. A three-dimensional part can be created by welding new foil layers on top of the previous layers and selectively machining away unwanted materials [1,2]. The UAM process is highly attractive due to its ability to join dissimilar or difficult-to-weld materials such as Al-Ti [3–6], Al-Cu [7,8], Steel-Ni [9], Steel-Ta [10], and Ni-Au [8,11], while also creating unique engineering components such as strengthened composites [12], unique cooling channels [13], and structures with embedded sensors [14,15].

UAM bonding occurs through a high strain rate (10^5 s^{-1}) [16,17] severe plastic deformation process. Shear deformation is applied from an ultrasonic welding horn, known as a *sonotrode*. The sonotrode applies a

force to the top of the foil and oscillates at a high frequency (20 kHz). The horn then travels down the length of the material bonding the two foils (Fig. 1). The shear deformation causes surface asperities to yield and collapse and breaks up surface oxides. Once the mating surfaces are atomically clean, they can bond at relatively low temperatures. A full description of the UAM process can be found in the ASM handbook [1, 2].

The methods of extracting the mechanical properties of UAM components include shear [4,18], tensile [17,19], microhardness [20–22], and nanoindentation testing [10,23,24]. Shear tests are often used for initial investigations of UAM bonding strength, as recommended by the American Welding Society for brazed and bonded joints [25]. Build (z-direction) UAM tensile tests are extremely time consuming to fabricate, without providing any additional information than shear tests, as they only effectively test the weakest interface [26]. Tensile testing in

[☆] This manuscript has been authored by UT-Battelle, LLC under Contract No. DE-AC05-00OR22725 with the U.S. Department of Energy. The United States Government retains and the publisher, by accepting the article for publication, acknowledges that the United States Government retains a non-exclusive, paid-up, irrevocable, world-wide license to publish or reproduce the published form of this manuscript, or allow others to do so, for United States Government purposes. The Department of Energy will provide public access to these results of federally sponsored research in accordance with the DOE Public Access Plan (<https://www.energy.gov/downloads/doe-public-access-plan>).

* Correspondence to: 323 Zeannah Engineering Complex, Knoxville TN 37996, United States.

E-mail address: mpagan1@vols.utk.edu (M. Pagan).

<https://doi.org/10.1016/j.addma.2022.103228>

Received 17 June 2022; Received in revised form 13 October 2022; Accepted 13 October 2022

Available online 21 October 2022

2214-8604/© 2022 Elsevier B.V. All rights reserved.

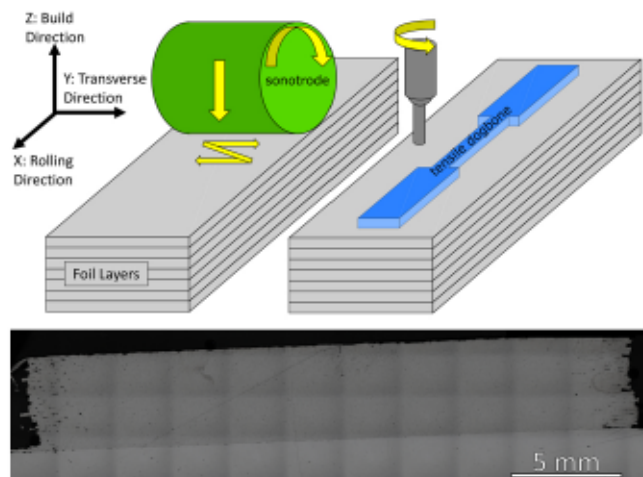


Fig. 1. Schematic overview of UAM bonding along with the tensile dogbones. Individually bonded foil layers can be seen in the optical overview image.

the longitudinal direction (rolling, x-direction) provides the most detailed information of the total build mechanical properties [17,19,27]. Indentation studies coupled with microscopy studies (in imaging and/or diffraction mode) provide valuable localized information about UAM foil-foil interfaces. Indentation testing has found that UAM builds typically have a local increase in strength at well bonded foil-foil interfaces [10] along with a decrease in the pattern quality from electron backscatter diffraction (EBSD) [21,22]. The decrease in EBSD pattern quality is associated with a dynamic recrystallized structure at the interface. The dynamic recrystallized structure results in reduced grain sizes and elevated dislocation densities [16,17,28]. Finite element modeling has also suggested the imposed plastic deformation refines the grain structure and increases dislocation density [29]. The force from the sonotrode on the top surface of a foil could also further increase the dislocation density as compared to the bottom of a foil [30]. Recent studies suggest that observed nanometer sized voids at UAM interfaces [8,24] could potentially also increase the strength through dispersed dislocation barrier effects [31].

Previous tensile testing of UAM builds from Al 6061 H-18 was reported by Sridharan et al. [19]. The tensile tests were performed in the build (z) direction and the in-plane (x or y) direction, then compared against bulk properties. The authors observed a 25% reduction in yield stress in the in-plane direction as well as an 84% reduction of yield stress in the build direction, and therefore, suggested that shear bands and microvoids were created at the interfaces. When the interface experiences a tensile load, the microvoids coalesce, create voids, and crack, resulting in brittle failure. Schick et al. [17] reported on Al 3003 H-18 tensile testing performed in the in-plane direction. This revealed a decrease in build strength as compared to bulk values. The authors suggested that the strength decrease was related to a large fraction of non-contact parabola shaped voids. The voids reduce the load bearing cross-section and increase the stress concentration intensity factor. Tensile testing in this current study is performed in the rolling (x) direction to compare with these previously reported results. The orientation of the tensile dogbones, with respect to the sonotrode and foil-foil interfaces, is shown in Fig. 1.

Additionally, the high strain rate plastic deformation UAM process can produce significant changes to the microstructure of structural materials. During plastic deformation, the creation of dislocation structures and point defect vacancies have been classically postulated by Friedel [32], Setiz [33], and others [34], although there has been a lack of strong experimental evidence regarding the formation of vacancies in materials during significant plastic deformation. UAM provides a convenient vehicle for studying the microstructure evolution and potential vacancy creation during high strain rate deformation. Chen et al.

[35] performed ultrasonic welding on a T4 tempered Al 6111 structure. Using modeling, hardness measurements, and electron microscopy, the authors observed a heat affected zone and precipitate structure at the foil-foil interfaces that increased during an 8-month period. The authors noted that the post weld aging occurred much faster than expected, which corresponds to a concentration of lattice point defect vacancies over 100 times larger than expected. Other authors investigating UAM bonding have noted large vacancy concentrations at the interfaces, which can lead to significant effects such as enhanced elemental inter-diffusion and interface strengthening effects [8,24]. Lattice defect changes during UAM have not yet been associated with large scale mechanical properties such as tensile testing. Additionally, various states of pretreating material, following ASM standards [36], prior to UAM have yet to be characterized. These pretreatments, ranging from annealing to T4 tempering, can alter the thermomechanical energy state of the material and grow energetically favorable precipitates. This research attempts to address how various pretreatments affect the microstructure of material created by UAM, and how these microstructure changes affect the built material's mechanical strength.

2. Experimental methods

2.1. Aluminum (Al 6061) and UAM processing

Al 6061 foils were initially received in the H-18 condition, prior to the welding pretreatment. The composition mass percent provided by the supplier is: 98% Al, 1% \pm 0.2% Mg, 0.6% \pm 0.2% Si, 0.195% \pm 0.155% Cr, 0.15% max Mn, 0.7% max Fe, 0.275% \pm 0.125% Cu, 0.15% max Ti, 0.25% max Zn. The aluminum was annealed into the "O" condition following ASM standards for heat treatment of Al 6061 [36] by increasing its temperature to 415 °C for three hours, then slowly cooling to room temperature (with a rate of -10 °C/hour). These foils are now referred to as *O Foils*. This slow cooling allows the aluminum to reach an equilibrium phase distribution at room temperature. Additional Al 6061 samples were tempered into the "T4" condition. Per ASM standards [36], T4 tempering was achieved by increasing the temperature to approximately 530 °C, holding it for one hour, followed by quenching in water. This should lock the phase distribution at \sim 530 °C. These foils are now referred to as *T4 Foils*.

The pretreated foils (\sim 150 μ m thick and 1 in. (25.4 mm) wide) were bonded to an Al 6061 T4 condition baseplate using a SonicLayer 4000 UAM system, with a vacuum chuck used to secure the weld substrate. Before UAM welding, the baseplate was first recovered using an endmill to ensure a flat build surface and then cleaned with alcohol to remove possible contamination. Texturing was then applied to the baseplate to help improve welding quality. This was performed by rolling the sonotrode over the surface while applying ultrasonic vibrations without a foil. The process parameters for bonding the samples were selected to optimize the welding for each treatment. For welding the *O Foils*, the UAM processing parameters used a normal force of 4000 N, a weld speed of 200 in./min (84.7 mm/sec), an amplitude of 33 μ m, and a baseplate temperature of 24 °C. For the *T4 Foils*, the UAM processing parameters used a normal force of 4000 N, a weld speed of 100 in./min (42.3 mm/sec), an amplitude of 36 μ m, and a baseplate temperature of 66 °C.

The tensile samples were subsize dogbones (gauge length 4 in. (101.6 mm)) machined out using a 0.125 in. (3.175 mm) diameter endmill in the x-direction orientation (Fig. 1). To achieve a nominal tensile sample thickness target of 0.05 in. (1.27 mm), the *T4 UAM* dogbones contained twelve bonded *T4 Foils*, and the *O UAM* dogbones contained fifteen bonded *O Foils*. The difference in number of foils is due to the reduction of foil thickness during UAM for the two tempers. The specimens were machined out entirely within the bonded foil regions. All tests were performed at room temperature on an MTS C43.504 load frame in conjunction with MTS wedge grips. The load frame was operated in displacement control mode at a crosshead speed of 1.27 mm/min (initial strain rate of 2.1×10^{-4} s $^{-1}$). The axial load was measured by a 5 kN

range load cell. To measure dogbone strain, a digital image correlation (DIC) system by Correlated Solutions Inc. was used with a virtual extensometer of 1 in. (25.4 mm) surrounding the break. Four tensile samples were used for each case, and the results are shown in Fig. 2. Identical samples were created to extract tensile specimens and preserved for microstructure analysis. The remaining microstructure characterizations, as described below, were performed in the same samples at adjacent locations for both the O UAM and T4 UAM conditions.

2.2. Nanoindentation

Nanoindentation experiments between the 1st and 2nd foil layers were performed on a KLA iMicro instrument using a Berkovich indentation tip with the shallow depth nanoblitz method [37]. The nanoindentations used a peak load of 1.15 mN. This corresponds to a peak indentation depth of 120–200 nm, depending on the location and hardness in the material. The three-dimensional nanoblitz hardness contour profiles were converted into average hardness line profiles by averaging the measured hardness at regular intervals away from the foil-foil interfaces. The y-error bars on the hardness line profiles represent one standard deviation from the average hardness, and the x-error bars represent the indent spacing.

Large depth nanoindentations were performed using the continuous stiffness method (CSM) [38–40] in the middle of the 1st bonded foil and at the interface between the 1st and 2nd foil. There were at least twenty-five CSM indents performed in the bulk foil regions, and their average and standard deviation are reported. There was difficulty in accurately indenting on the interface due to its small width. Indent arrays were performed near the interface and the indents with a higher hardness are reported as the interface. The CSM indents were performed approximately six months after the structural investigation by transmission electron microscopy (TEM), therefore some natural aging of the aluminum might have occurred. All CSM indents were performed using a Berkovich tip to a peak load of 20 mN, using a strain rate of 0.20 s^{-1} , an oscillation frequency of 110 Hz, and an oscillation amplitude of 2 nm. All indents were performed with sufficient spacing between indents to reduce overlap of their plastic strain fields [41].

2.3. Microstructural characterization

Computational thermodynamics of the materials were performed using the Thermo-Calc® program [42]. Samples for microscopy analysis were prepared by cold mounting in epoxy followed by mechanical polishing using standard metallography techniques. Optical microscopy was performed on a Leica DM4000M using brightfield mode with digital

image stitching. For electron microscopy, charging effects were reduced by sputtering a few nanometers of carbon coating onto the surface of the samples. Scanning electron microscopy (SEM) images were taken using a Zeiss Evo with a LaB₆ filament. For fractography, the SEM working distance was maximized to increase the depth of field (DOF) across the surface [43].

Samples for X-ray diffraction (XRD) were prepared using a low-speed saw. For the UAM bonded samples, a cross section of approximately five foils was sectioned for analysis. X-ray diffraction was performed at the 11BM beamline at the Advanced Photon Source (APS) ($\lambda = 0.4581 \text{ nm}$) [44] using Debye-Scherrer geometry, and analysis of the scans was performed using standard Rietveld Refinement techniques [45,46].

Samples for transmission electron microscopy (TEM) were extracted from the bonded material at interfaces between the first and second foil layers, and at locations distant from any obvious bonding voids. These TEM lamella samples were prepared using a focused ion beam (FIB) / SEM Zeiss Auriga using standard procedures with a gallium-ion beam at voltages from 30 kV to 5 kV and with a beam current progressively decreasing from 2 nA to 50 pA. Finally, the TEM lamellae were lifted from the sample surface using an OmniProbe and welded to a copper grid for further TEM analysis. The microstructure of the FIB lamellae was analyzed in a ThermoFisher Titan 60–300 Scanning Transmission Electron Microscope (STEM) operated at 300 kV. The images were taken with a camera length of 460 mm with an HAADF collection angle of 21–136 mrad. A Super-X™ energy dispersive x-ray spectrometer (EDS) was used to obtain compositional maps. The spectrum images obtained were quantified using the Velox™ software. The grain size from the STEM image was calculated using the Heyn's line intercept method [47], and the dislocation density was determined using the line-cut method [48]. It should be noted that the TEM analysis was performed approximately two months after other characterizations. Therefore, additional natural aging of the aluminum could have occurred resulting in slightly larger precipitate sizes. Additionally, it should be noted that the TEM samples were not taken directly below the nanoindentations. This means material variations and uncertainties are present, and they should be considered when comparing the results.

3. Results

3.1. Tensile testing

This study demonstrates that considerable strengthening can develop in materials created by ultrasonic additive manufacturing (UAM). As discussed previously, UAM creates structures by bonding foils together. To discuss the material changes that develop, materials characterized

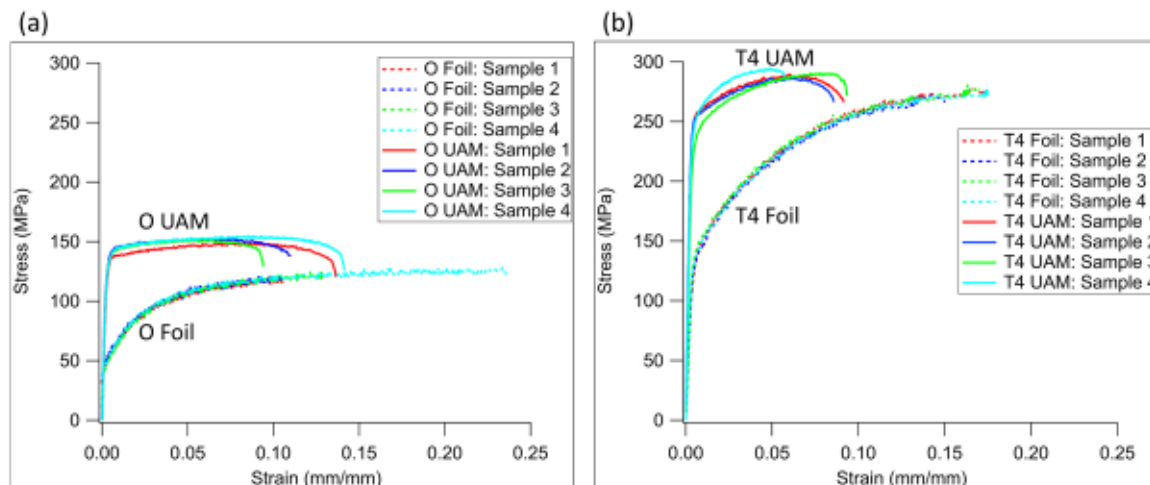


Fig. 2. Tensile testing results a) Al 6061 O, b) Al 6061 T4.

prior to the UAM process will be referred to as foil material, and materials characterized after bonding will be referred to as being in the UAM geometry.

Individual tensile stress-strain curves (from the x-direction) are shown in Fig. 2 for the *O Foil* samples, the *O UAM* samples, the *T4 Foil* samples, and the *T4 UAM* samples. The tensile testing numbers for each sample represent the sequential number for each sample used in tensile testing. Engineering stress, which uses the original cross-sectional area, was used for the tensile testing mechanical property analysis. Therefore, any small differences in cross-sectional area are normalized during analysis. The stress-strain curves demonstrate that the initial Al 6061-T4 material is harder than the initial Al6061-O material. Additionally, the UAM bonding causes an increase in strength for both sets of material. This is in direct contrast to the decrease in strength due to UAM in Al 6061 H-18 material observed by Sridharan et al. [19]. The rationalization of the increase in strength after UAM bonding is the focus of this work.

Mechanical properties from the tensile testing are summarized in Table 1. The average and standard deviation from each set of samples is listed along with standard reference values. Notably, the strain hardening coefficient from the *O UAM* samples and the *T4 UAM* samples, as determined using Considere's criteria [49], is quite low. This indicates the materials have near perfect plastic deformation prior to failure. The elastic moduli of the *O UAM* and *T4 UAM* samples are within 10% of the standard values for Al 6061, indicating these tests are valid within reasonable experimental error [50,51]. The elastic modulus is quite low for the foil samples demonstrating the difficulty in tensile testing thin foil samples. It should be noted that these tensile properties might not have perfect comparison with the published literature of standard Al 6061 temper tensile properties [52–54]. This is due to several factors including the geometry of the subsize tensile bars that were used in this experiment. Additionally, the standards for aluminum temper designations describe that annealing processes should remove all prior heat treatment or cold rolling [52]. As shown in the sections below, some distinct microstructure features remain from the foil rolling process prior to UAM bonding. However, as noted previously, the purpose of this study is to understand how the mechanical properties of these materials changed due to the UAM process, and to understand the microstructures that created these property changes.

3.2. Characterization of Al 6061 O Foil (before UAM)

The baseline *O Foil* material was analyzed using scanning transmission electron microscopy (STEM). Fig. 3 is a STEM high angle annular dark field (HAADF) image of the Al 6061 *O Foil*. A dislocation cell wall structure (cell size approximately 1 μm) is observed by the higher contrast spaghetti lines (dislocations). The cell walls contain a significant concentration of dislocations, while cell interiors have a low density of dislocations. A dislocation cell structure is often associated with microstructures after significant plastic deformation [57]. The cell wall structure could be present due to the rolling processing which was required to roll the aluminum into a thin foil ($\sim 150 \mu\text{m}$). The subsequent annealing process (to create the *O* condition) might not have been sufficient to remove the dislocation network. From Fig. 3a, the dislocation density is $1.06 \times 10^{10} \text{ cm}^{-2}$ which is representative of a typical

dislocation density for moderately cold worked materials.

In addition to the observed dislocation network, precipitates of various sizes and a single grain boundary are observed. In the STEM image (Fig. 3a), a grain boundary from the top left towards the bottom right can be identified. Since the viewing window is approximately $60 \mu\text{m}^2$, the grain size must be quite large ($> 100 \mu\text{m}^2$). The bright high-contrast objects in this HAADF-STEM image are likely the precipitates (with a high combined atomic number of $Z = 38$) in the aluminum matrix (atomic number $Z = 13$). These precipitate objects are mostly located in the center of dislocation cell walls and grain boundaries. Fig. 3b is a magnification of the central grain boundary, as highlighted in Fig. 3a. The grain boundary cuts through the center of a large precipitate. In this viewing window the precipitates' chemical compositions were identified using energy dispersive X-ray spectroscopy (EDS) analysis (see Supplementary Fig. S1). Some of these precipitates contain magnesium and silicon, suggesting a Mg_2Si precipitate. Other precipitates contain concentrations of iron, manganese, and chromium. The quantified spectrum images indicate that the precipitates pinning dislocation cell walls are Mg_2Si . These precipitates are spherical and ellipsoidal in shape, with a characteristic Feret diameter of approximately 200 nm and an average spacing L of 1.02 μm . The volume fraction v_f of the precipitates can be approximated as the volume of each precipitate divided by the three-dimensional average spacing between each particle.

$$v_f = \frac{V_p}{L^3} \quad (1)$$

The volume fraction of Mg_2Si precipitates is 0.00396. Using the EDS spectrum across the entire imaging window, the calculated composition mass percent with associated fit error is 98.3 \pm 0.1% Al, 1.4 \pm 0.4% Mg, 0.1 \pm 0.4% Si, 0.1 \pm 0.6% Cr, 0 \pm 4% Mn, 0 \pm 0.7% Fe. This composition is slightly varied from the standard composition of Al 6061 [58] and that provided by the supplier (Section 2).

3.3. Characterization of Al 6061 O UAM

3.3.1. Microstructure and mapping of elemental compositions using STEM-EDS

An overview image of the bonded *O Foils* to create the *O UAM* sample can be seen in Fig. 1. Low magnification optical image stitching was performed to show the entire cross-section of the sample. After UAM bonding of the *O Foils*, the microstructure was significantly altered. A thin lamella of the *O UAM* interface is shown below (Fig. 4). The interface between two *O Foils* is indicated with the arrow in Fig. 4a. Although there is pronounced grain refinement within $\sim 100 \text{ nm}$ of the interface, regions located $200\text{--}300 \text{ nm}$ from the interface show a relatively large grain structure. The microstructure at regions 0.3 m away from the interface exhibit large grains with an average size of $620 \text{ nm} \times 300 \text{ nm}$ with large pinning precipitates, mostly at grain boundaries.

The interface microstructure was examined using HAADF-STEM (Fig. 4b) and TEM bright field (BF) imaging (Fig. 4c). The refined grain structure is clear at the interface, as extremely fine grains (100 nm \times 70 nm) are present within a region approximately 115–800 nm in width. The refined grain size is likely the result of a dynamic recrystallization event previously described at UAM interfaces [16,20]. In addition to the refined grain structures, there are regions of dark circles in the HAADF image and bright circles in the BF image. These regions could be voids or vacancy clusters. Vacancy clusters are present at the interface on grain boundaries and inside a large grain on one side of the interface. The vacancy clusters, which are preferential on only one side of the interface, could also be related to the non-uniform hardness increase across the interface observed through nanoindentation, as shown below.

It should be noted that the voids present could potentially be explained as a result of TEM sample preparation using FIB as well.

Table 1
Mechanical properties from tensile testing.

Sample	Yield Stress (MPa)	Ultimate Tensile Stress (MPa)	n	$n[55]$	E (GPa)	E (GPa) [56]
<i>O Foil</i>	46 \pm 5.1	126 \pm 3.0	0.13	0.158	22	68.9
<i>O UAM</i>	127 \pm 2.1	150 \pm 2.3	0.01		64	68.9
<i>T4 Foil</i>	137 \pm 1.4	277 \pm 1.9	0.07	0.069	32	68.9
<i>T4 UAM</i>	210 \pm 18.2	270 \pm 20.1	0.02		75	68.9

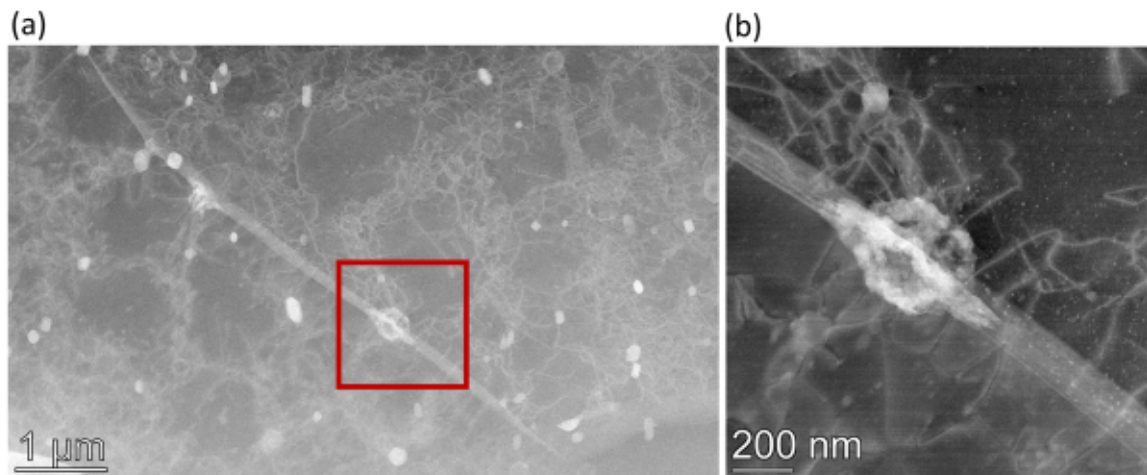


Fig. 3. STEM HAADF image of the Al 6061 O Foil microstructure. a) Dislocation cell structure, b) Grain boundary/precipitate from highlighted region.

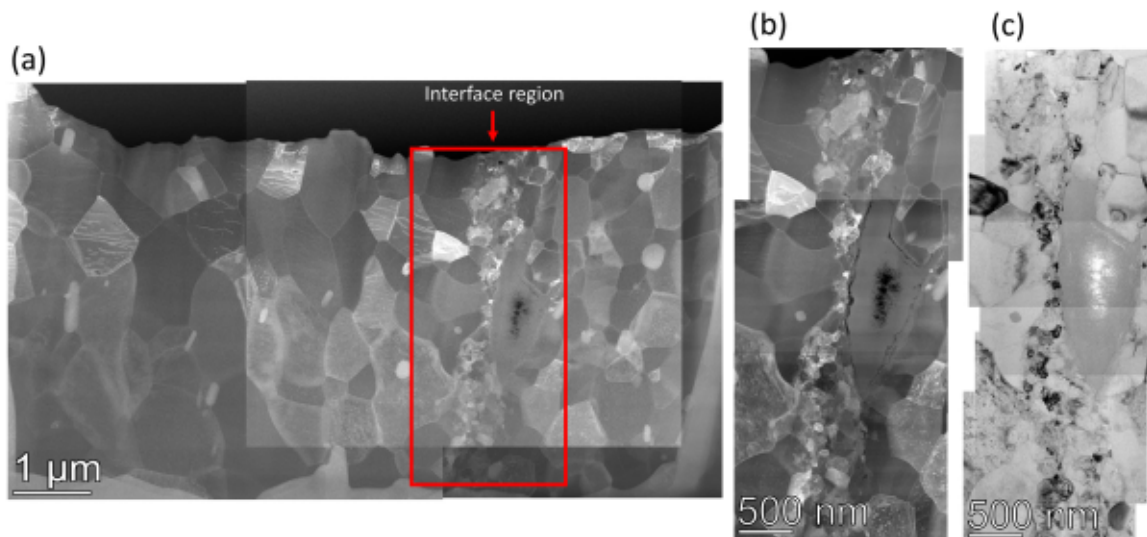


Fig. 4. STEM/TEM analysis of Al 6061 O UAM microstructure: a) STEM HAADF image of the lamella, b) STEM HAADF of the interface, c) TEM BF of the interface.

However, voids are not observed far away from the interface region. Additionally, there is elemental migration, as described below. Given this, the voids would more likely be associated with excess point defect lattice vacancies, which produced enhanced atomic diffusion, then combined into larger vacancy clusters. Vacancy clusters and accelerated diffusion have been observed as a result of severe plastic deformation [8, 59,60] and radiation effects [61–63]. Therefore, it is highly likely that the voids are associated with the UAM bonding process.

The precipitates have a plate-like morphology, appearing rod-like in the two-dimensional representation shown. The element distribution in these precipitates in the interface region can be identified using EDS, shown in Fig. 5 and Fig. 6. EDS maps identify magnesium, silicon, iron, manganese, and chromium content. Fig. 6a is a combined EDS map of the interface with two EDS line profiles as indicated. Fig. 6b demonstrates the local concentration of elements at the top right precipitate. This concentration of elements suggests a $MgSi$ or Mg_2Si composition. Magnesium and silica have only a small difference in characteristic X-ray energy, therefore slight overlapping of the tails could occur. This slight energy overlap and X-ray absorption effects could convolute the exact composition [64]. Since the Mg_2Si structure is the only stable Mg-Si configuration [65], it can be confidently assumed that these precipitates are Mg_2Si . Fig. 6c demonstrates that the bottom left precipitate has a local concentration of elements that trend towards a

configuration of an $Al_9Fe_2Si_2$ and/or $Al_{13}Cr_4Si_4$ precipitate. Both these stoichiometries are thermodynamically stable in the Al 6061 O condition [42]. The intermetallic iron or chromium precipitates result from impurities in the aluminum casting process, and they do not significantly contribute to strengthening [66].

Although the non-strengthening precipitates of iron, manganese, and chromium appear mostly unaffected by the UAM process, the Mg_2Si precipitates appear significantly different. There are fewer Mg_2Si precipitates present after bonding, and only one remains within 1 μm of the interface. The magnesium appears broken up and dissolved back into the aluminum at the interface, while several large pockets of silicon remain. This suggests that the magnesium diffused and dissolved more quickly than the silicon.

3.3.2. Failure analysis after tensile testing using fractography

The fracture surface of the O UAM sample (Fig. 7) can shed more light on the deformation response of this material. The overview image (Fig. 7a) demonstrates approximately fifteen foils were used in the tensile testing. Further magnifications on the fracture surfaces (Fig. 7b & Fig. 7c) show that ductile fracture is present during deformation. Significant reduction of area occurs prior to fracture, and the final fracture appears near the center of the foil. The chisel edge/knife edge fracture occurs within each of the fifteen individual original foils. Dimples are

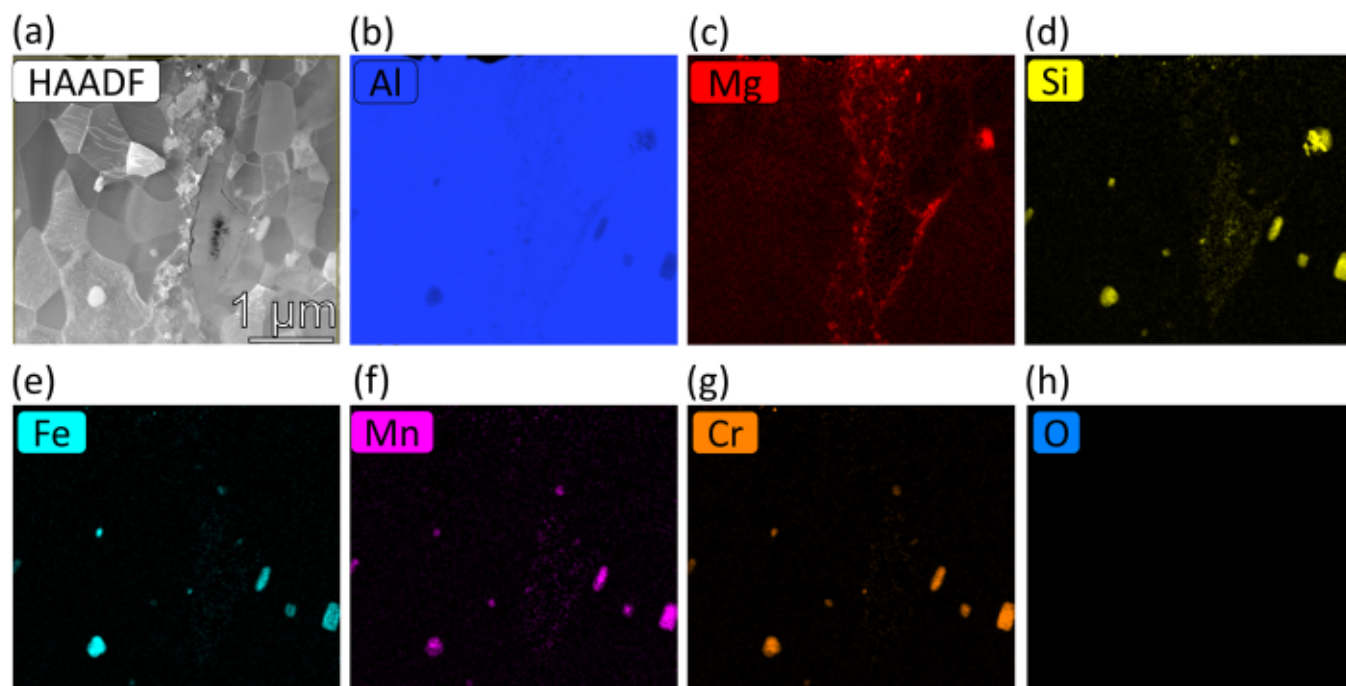


Fig. 5. STEM / EDS map of the Al 6061 O UAM interface. a) STEM HAADF image, b) EDS map of aluminum, c) EDS map of magnesium, d) EDS map of silicon, e) EDS map of iron, f) EDS map of chromium, g) EDS map of oxygen.

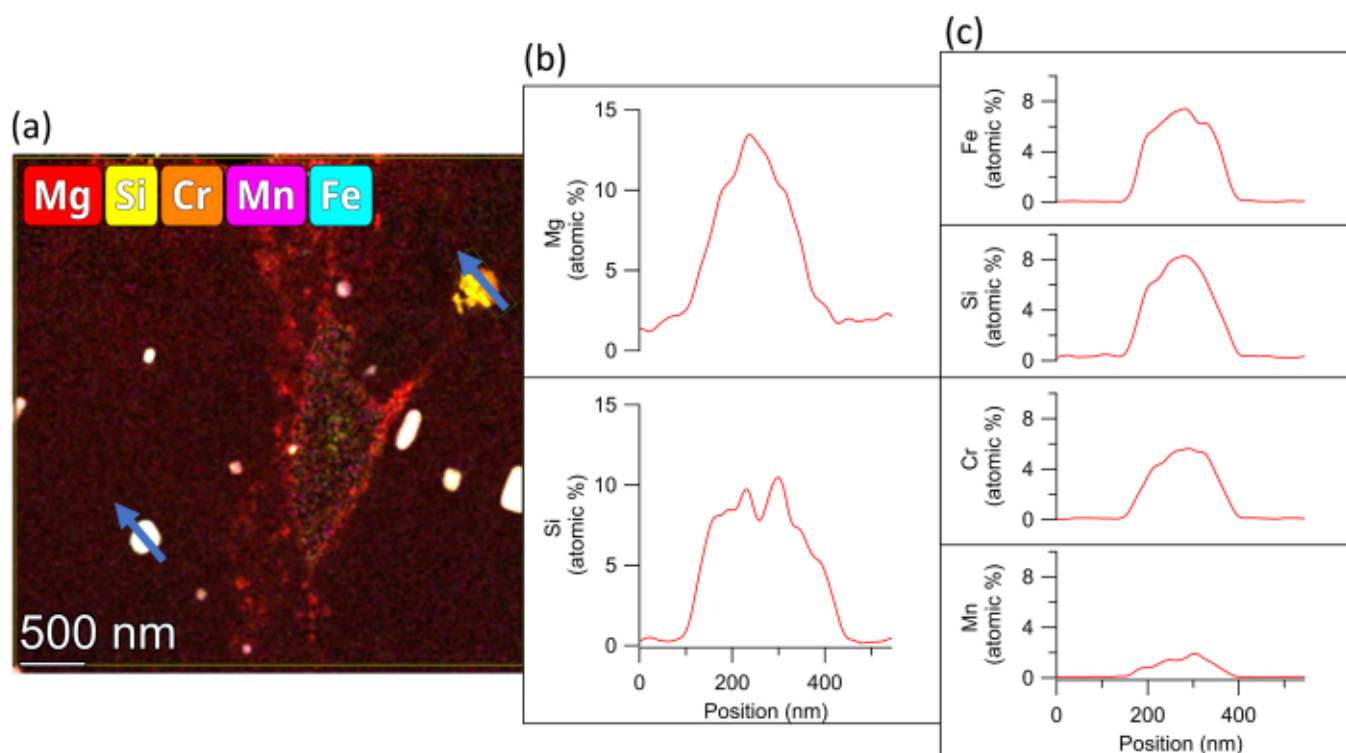


Fig. 6. STEM / EDS line scan of Al 6061 O UAM interface. a) Combined EDS maps with indicated line scans, b) EDS line scan of top right Mg_2Si precipitate, c) EDS line scan of bottom right Fe-Si-Cr-Mn precipitate.

present throughout the fracture surfaces, which are typically associated with deformation at precipitates or other inclusions [67,68].

As noted in the stress-strain curves, the O UAM samples had significant necking prior to failure. Since the middle of the foil necked more than the interfaces, it is likely the interface was harder with reduced ductility. This caused it to fail faster, then upon further loading the foils

continued to deform and neck until they ultimately fractured. The foils do not appear to have separated from each other; therefore, the potential increase in hardness at the interface was not significant enough to cause separation.

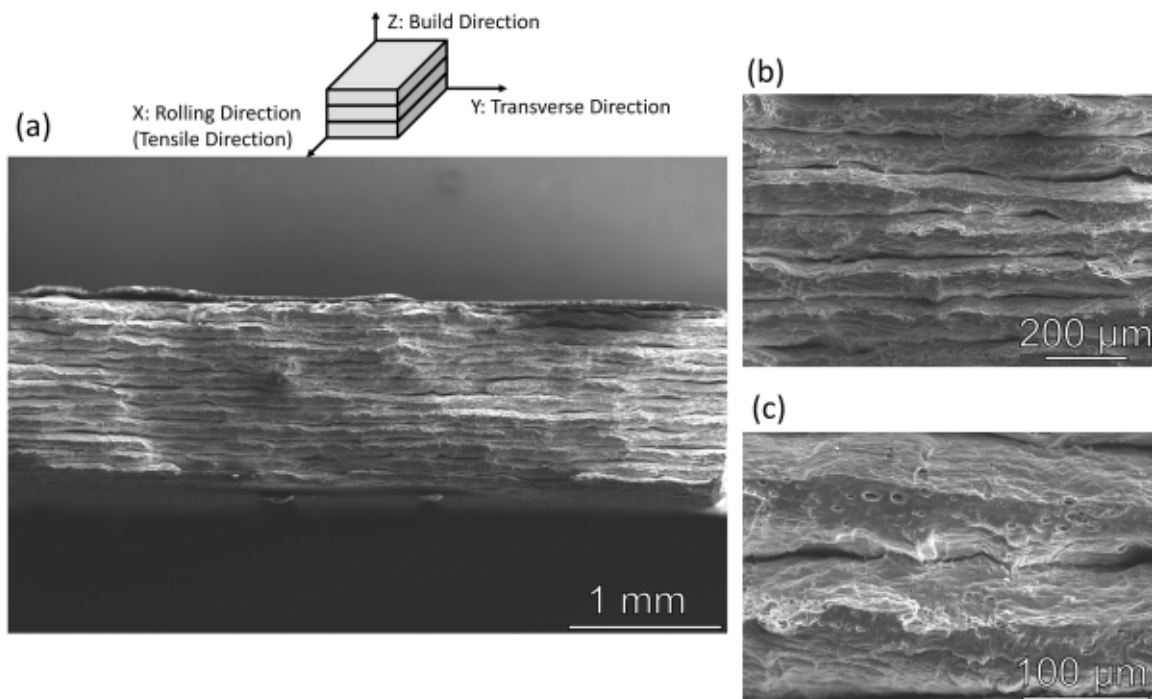


Fig. 7. Tensile fracture surface of the O UAM sample. a) Overview of the entire fracture surface, b) Magnification of several foils, c) Further magnification of two foils and their interface.

3.3.3. Site-specific hardness measurements using nanoindentation

To quantify the local mechanical properties, nanoindentation was performed. The hardness was compared across the interface using a shallow depth nanoblitz array and large depth continuous stiffness mode (CSM) array at the interface and bulk foil region (Fig. 8). The nanoblitz hardness contour (Fig. 8a) is rotated for visual aid so that the top of the build is located at the top of the image. The contour demonstrates that the interface is much harder than the bulk foil region. A normalized line of the indents (Fig. 8b) is provided to demonstrate the average and standard deviation of the hardness. The SEM image of the indent array (Fig. 8c) is rotated to correspond to the hardness contour plot. The sizes of the indents (from the SEM image) are approximately 30% smaller at the interface as compared to the bulk foil regions. Since hardness is inversely proportional to the indent area, this indicates the interface is harder than the bulk foil regions, although the indent size effect should also be considered for detailed quantitative hardness analysis. The interface between the foils, as viewed from nanoindentation, appears asymmetric. There is a gradual rise of hardness on the top of the bottom foil, then a sharper decrease in hardness on the bottom of the top foil. The region of the material with the highest hardness is the interface. From the nanoindentation spatial mapping, it has a width of approximately $12 \mu\text{m} \pm 2 \mu\text{m}$. The CSM indentations performed on the interface and in the bulk foil regions are shown in Fig. 8d. Although the interface is harder than the bulk foil region, there is also a depth dependence to the nanoindentation hardness values. Additional analysis must be performed to quantify the hardness difference at the interface and bulk regions. This is discussed further in the section below. Several white particles are observed on the sample surface in Fig. 8c. The indentation pattern on the aluminum sample is underneath the white particles, which indicates these particles are not a precipitates phase that is part of the aluminum. These contaminant particles likely fell onto the surface of the material during sample transfer between the nanoindentation testing and the microscopy characterization.

3.3.4. Variations in crystallography using XRD

Crystallographic strain can be understood using X-ray diffraction (XRD). The diffraction patterns comparing the O Foil and O UAM

samples are shown below in Fig. 9. The aluminum and the Mg_2Si phases are identified in Fig. 9a. The existence of these phases corresponds to the previous results shown above. The XRD scan of the O UAM samples encompassed a relatively large area, across at least five foils and interfaces. Therefore, any potential phase changes that could occur at the interfaces would be too small to be observable. It should be noted that the diffraction pattern is plotted on a logarithmic scale. Most diffraction peaks are labeled, and the remaining unlabeled peaks are so small in intensity that their phase fraction is negligible.

Although local phase changes at the interfaces would be imperceivable, diffraction broadening from lattice strain in the materials can be observed. An arbitrary peak is chosen to observe the diffraction broadening. The aluminum $\{111\}$ peak is chosen because it is the strongest peak. The aluminum $\{111\}$ peak from the O Foil and O UAM samples are shown normalized and superimposed to demonstrate the diffraction broadening that occurs (Fig. 9b). The O UAM sample has a broader aluminum peak than the O Foil sample. This indicates the O UAM sample has more crystallographic lattice strain than the O Foil sample. Additionally, following Rietveld refinement on the O Foil and O UAM samples, the generalized mean microstrain values are 1036 and 1607, respectively. This indicates that the aluminum has an increase in lattice strain after the UAM process, likely from additional lattice distortions such as dislocations.

3.4. Characterization of Al 6061 T4 Foil (before UAM)

A STEM image showing the typical microstructure of the T4 Foil prior to UAM bonding is shown in Fig. 10a. The bottom half of the lamella seems slightly too thick for electron transparency, indicated by weak contrast changes between microstructure features. The top half of the lamella shows dislocation tangles and several precipitates with a plate or rod like morphology. Fig. 10b, which is a magnified image of the highlighted area shown in Fig. 10a, shows one large precipitate, several smaller precipitates, and dislocation tangles homogeneously distributed throughout the sample. From Fig. 10a, the dislocation density is $1.68 \times 10^{10} \text{ cm}^{-2}$. The precipitate's chemical composition, using EDS analysis (Supplementary Fig. S2) demonstrates several large regions of

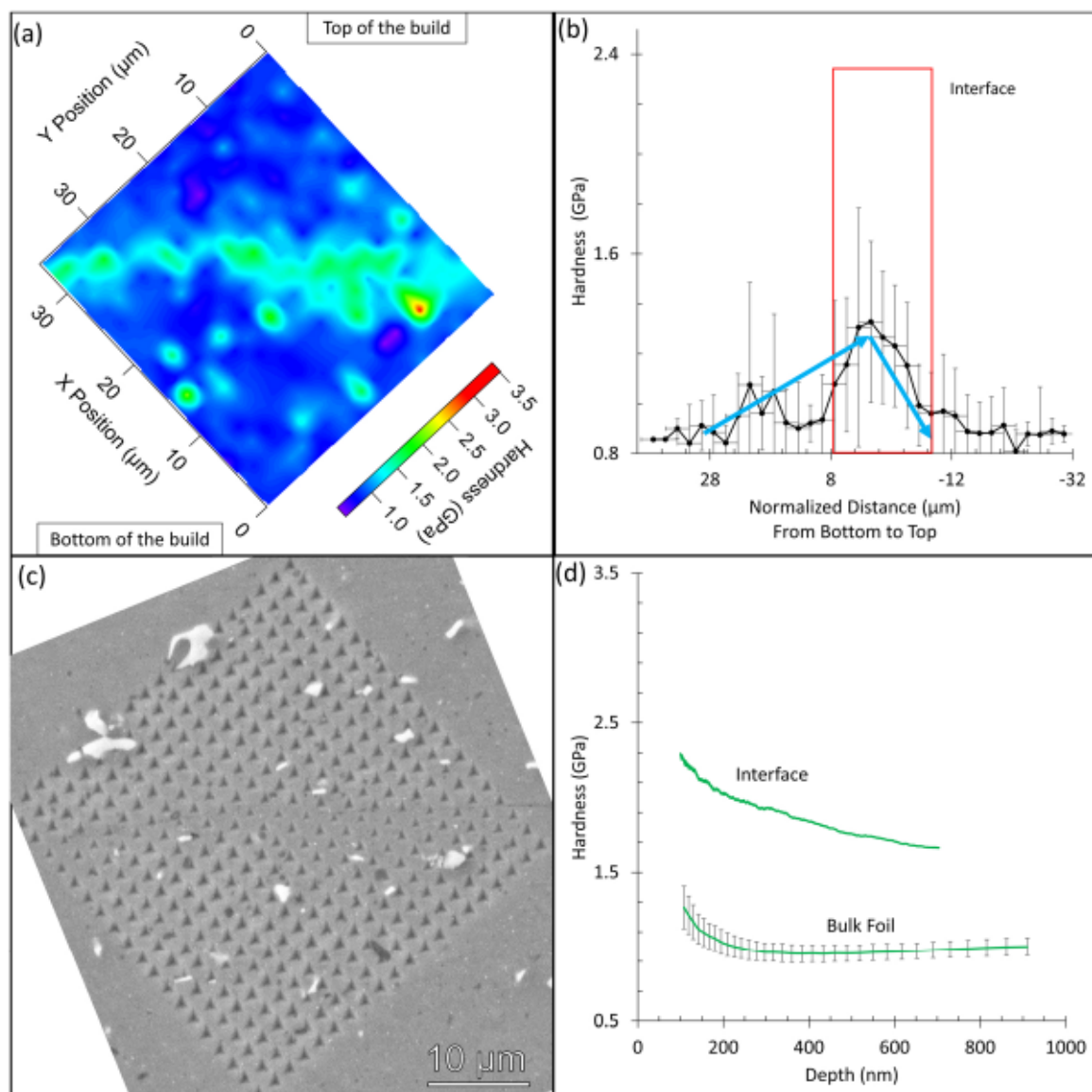


Fig. 8. Nanoindentation hardness map of the O UAM build. a) Nanoblitz hardness map, b) Average hardness line, c) SEM image of the indent array, d) Hardness vs depth for CSM indents.

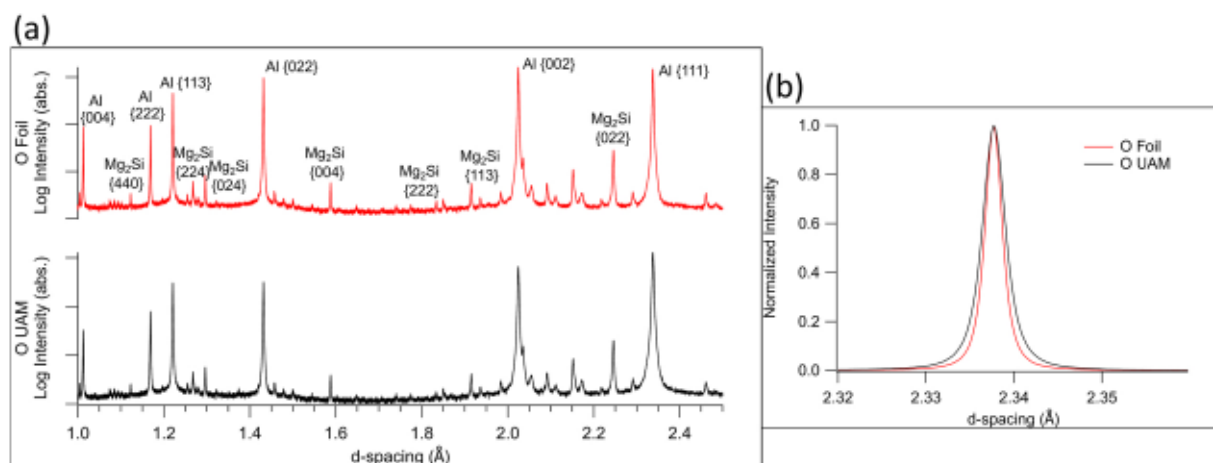


Fig. 9. XRD of the O Foil and O UAM samples. a) Diffraction patterns, b) Comparison of Al {111} peaks.

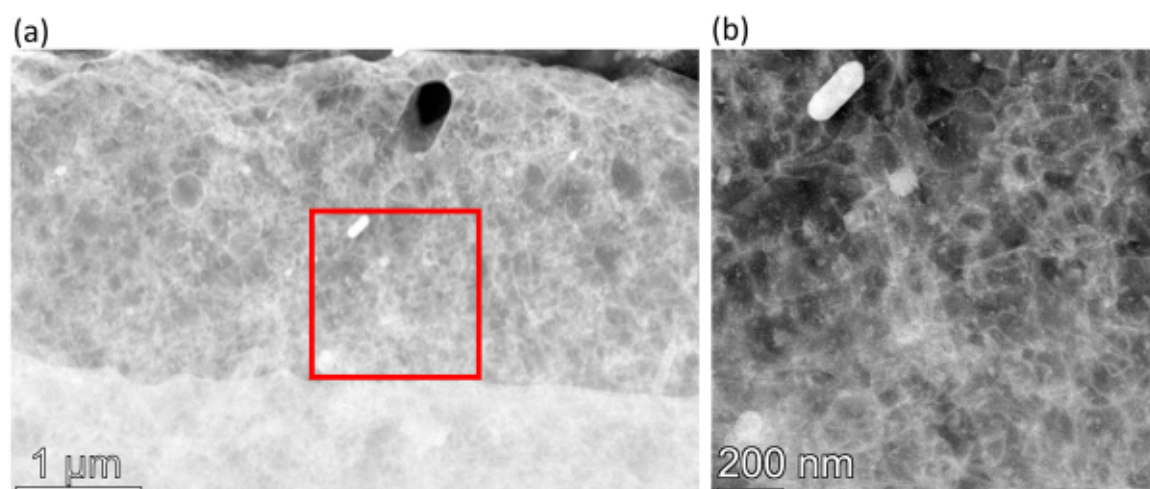


Fig. 10. STEM image of Al 6061 T4 Foil microstructure. a) HAADF image of entire lamella, b) HAADF of highlighted dislocation network.

magnesium and silicon suggesting a Mg_2Si precipitate. There are fewer precipitates in the lower half of the image, although this is likely due to the lamella being too thick, as noted previously. The large Mg_2Si precipitates have a spherical or ellipsoidal morphology. The T4 Foil has fewer precipitates than the O Foil, although the precipitates are larger (Feret diameter of 230 nm) with an average spacing of 1.70 μm and a volume fraction of 0.00148. Additionally, since the T4 Foil is quenched from a high temperature, it initially has a higher vacancy concentration than the O condition. This can lead to slow natural aging of the solute phase [36,55,69].

3.5. Characterization of Al 6061 T4 UAM

3.5.1. Microstructure and mapping of elemental compositions using STEM-EDS

After the UAM bonding process of the T4 Foils, the microstructure was analyzed using STEM (Fig. 11). The entire TEM lamella is shown in Fig. 11a. The microstructure several microns away from the interface is an equiaxed grain structure ($610\text{ nm} \pm 290\text{ nm}$). The interface between the T4 Foils is highlighted and magnified using a HAADF-STEM image (Fig. 11b) and a TEM BF image (Fig. 11c). The interface exhibits a refined grain structure ($120\text{ nm} \pm 80\text{ nm}$) within a region that is 210–450 nm in width. The grain size of the T4 UAM sample at the interface and in the bulk foil regions is statistically identical to the grain

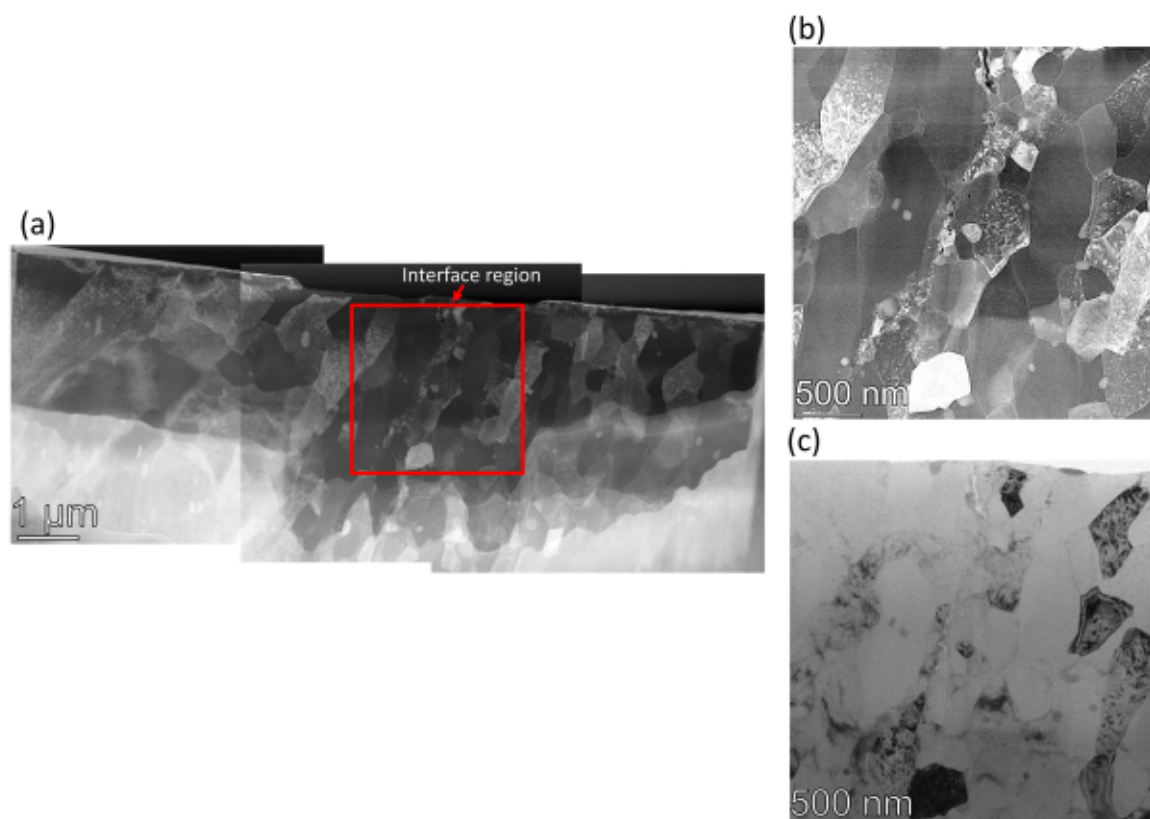


Fig. 11. STEM/TEM of Al 6061 T4 UAM microstructure. a) STEM HAADF image of the lamella, b) STEM HAADF of the interface, c) TEM BF of the interface.

size of the interface and bulk foil regions in the *O* UAM sample (see Fig. 4). The *T4* UAM sample has fewer identified precipitates close to the interface, as compared to before the UAM bonding. The remaining precipitates have a plate-like morphology (appear rod-like in the two-dimensional view). At the interface, there are also voids/vacancy clusters along grain boundaries and inside of grains, although there are fewer voids than in the *O* UAM sample.

The composition of the interface region is shown in EDS maps in Fig. 12. The non-strengthening Fe-Mn-Cr precipitates appear mostly unaffected. The compositional feature most notable is that the interface is strongly enriched in magnesium and oxygen. The few Mg_2Si precipitates in the foil prior to UAM bonding appear completely dispersed into the aluminum after bonding. The interface appears as a sink for magnesium segregation. It is likely that local silicon-rich regions are previous Mg_2Si precipitates. The Mg_2Si precipitates could have dissolved, the magnesium diffused away, and the silicon left behind. This composition of the *T4* UAM sample is qualitatively similar to the *O* UAM sample. The Mg_2Si precipitate decomposed, and Mg segregation occurred toward the interface. Unlike the *O* UAM sample, in the *T4* UAM sample oxygen was also detected at the interface, although it should be noted that oxygen is difficult to detect using EDS techniques [43,64].

3.5.2. Failure analysis after tensile testing using fractography

The overview fracture surface image (Fig. 13a) demonstrates there were approximately twelve *T4* Foils contained in the gage region for the tensile testing. Further magnifications of the fracture surfaces (Fig. 13b & Fig. 13c) show ductile fracture was present during deformation. As in the case of the *O* UAM sample, the *T4* UAM sample has dimples throughout the fracture surface suggesting precipitates were present. Although there appears to be reduction of area prior to fracture, it is less pronounced than in the *O* UAM sample, which is also indicated by the stress-strain curves (Fig. 2) and work hardening coefficient.

Unlike the *O* UAM sample, the *T4* UAM fracture surface shows that the foils separated. The separation of these foils after fracture suggests the interfaces were much harder than the bulk foil regions. As the total composite material deformed, the interface regions likely reached their yield point and plastically deformed before the middle of the foil. As the

material continued to deform, the foils broke away from each other to continue plastically deforming.

3.5.3. Site-specific hardness measurements using nanoindentation

Nanoindentation was performed on the *T4* UAM sample (Fig. 14). The low depth nanoblitz hardness contour (Fig. 14a) is rotated for visual aid so the top of the build is oriented on the top of the image. Like the *O* UAM interface (Fig. 8), the *T4* UAM interface is harder than the bulk foil regions. The normalized hardness line profile (Fig. 14b) shows the average and standard deviation of the nanoblitz hardness values. Compared with the *O* UAM sample (Fig. 8b) the *T4* UAM sample and interfaces are clearly harder than those in the *O* UAM sample. The SEM image of the indent array (Fig. 14c) is rotated to correspond to the hardness contour plot. From the image, the indents near the interface appear shallower than the indents further away into the bulk foil regions. Therefore, the hardness depth dependence should be addressed. Like the *O* UAM interface, the nanoindentation information from the *T4* UAM interface demonstrates asymmetry. There is a gradual hardness increase going from the bottom foil to the interface, then a sharper hardness decrease going into the top foil. The interface width, as determined by nanoindentation, is approximately $10 \mu m \pm 2 \mu m$. The CSM indentations on the interface and the foil bulk region (Fig. 14d) demonstrate that the hardness also has an indentation depth dependence. Evaluation of the hardness increase at the interface while removing the depth dependence will be discussed in the section below. Like the *O* UAM indentation array, several white contaminant particles are present on the image in Fig. 14c, although they did not affect the testing.

3.5.4. Variations in crystallography using XRD

The diffraction from the *T4* Foil and *T4* UAM samples have been observed using XRD (Fig. 15). The diffraction patterns of these samples are shown below in Fig. 15a with the aluminum and Mg_2Si phases identified. Like the XRD results discussed above, the large sampling volume here makes distinguishing phase differences between the interface and bulk foil regions very challenging.

The diffraction broadening of the aluminum phase can be observed

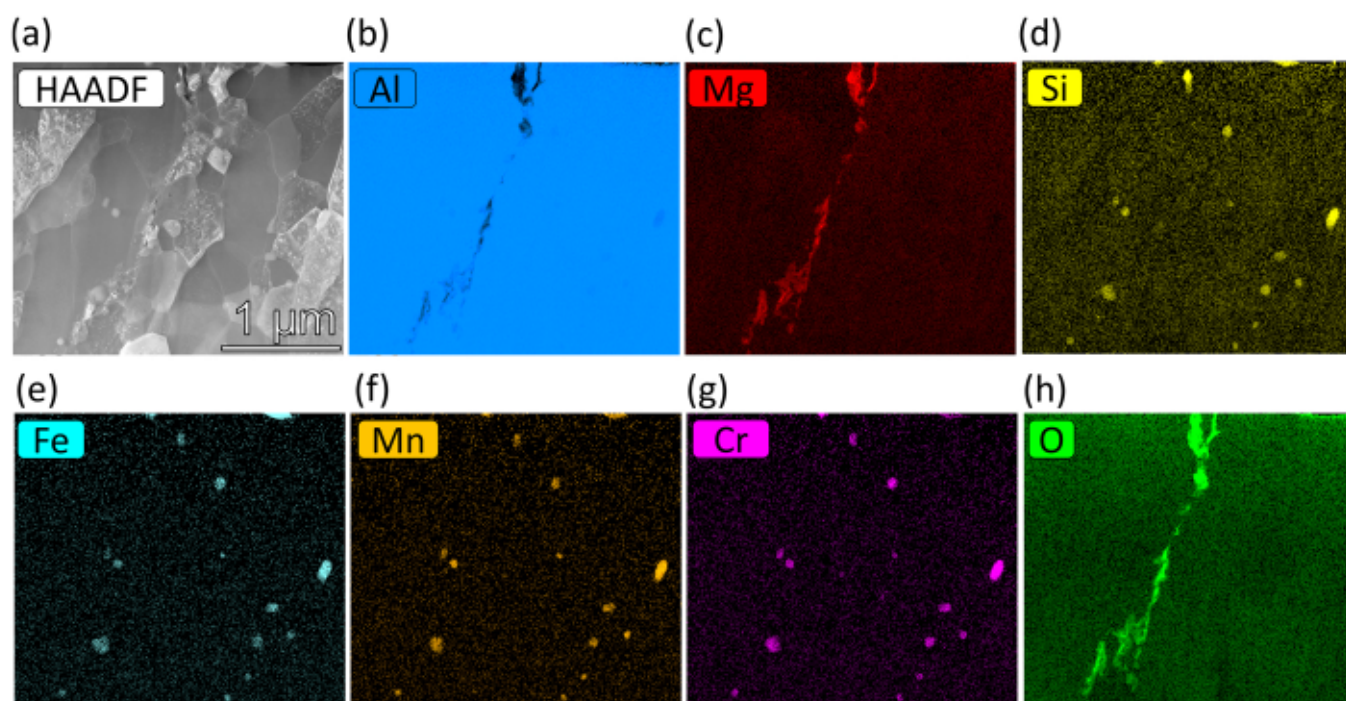


Fig. 12. SEM/EDS map of Al 6061 *T4* UAM microstructure. a) STEM HAADF image, b) EDS map of aluminum, c) EDS map of magnesium, d) EDS map of silicon, e) EDS map of iron, f) EDS map of manganese, g) EDS map of chromium, h) EDS map of oxygen.

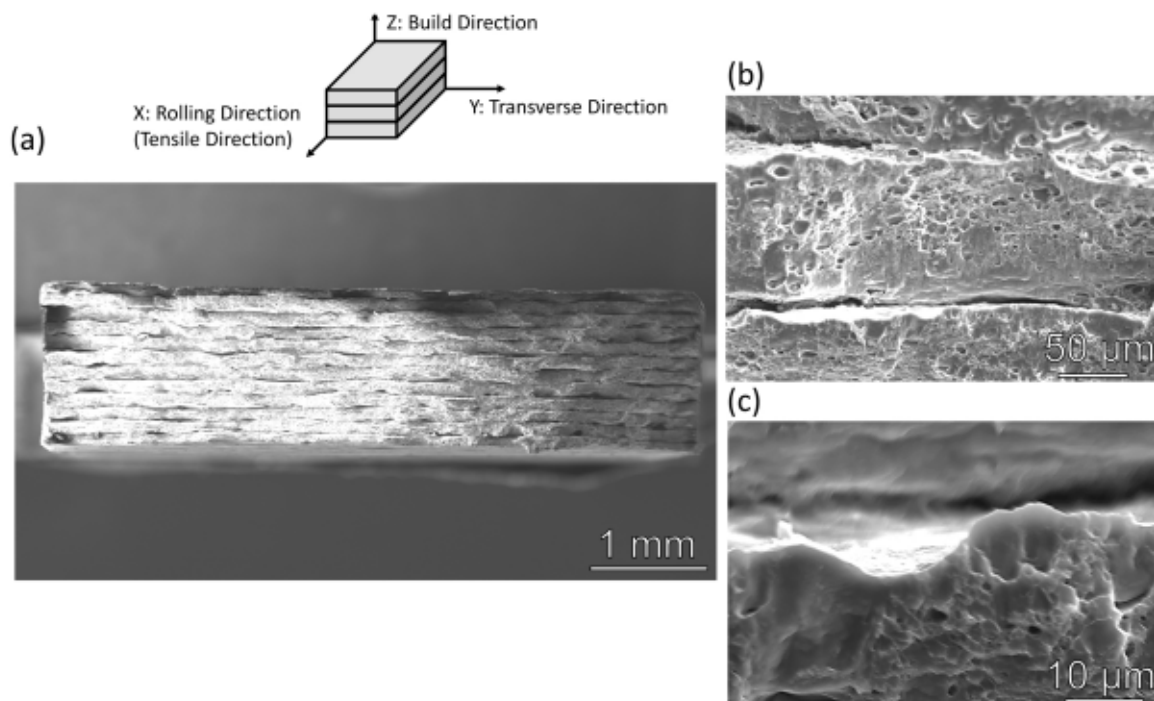


Fig. 13. Tensile fracture surface of the T4 UAM sample. a) Overview of the entire fracture surface, b) Magnification of several foils, c) Further magnification of two foils and their interface.

by focusing on a main aluminum peak. The aluminum {111} peak of the T4 Foil and the T4 UAM sample is normalized and superimposed to demonstrate the broadening between the samples (Fig. 15b). The T4 UAM sample has a broader aluminum peak than the T4 Foil sample. This means there is more crystallographic strain in the bonded sample than in the foil sample. Additionally, the generalized mean microstrain values of the aluminum in the T4 Foil and T4 UAM sample, as calculated by Rietveld Refinement, are 1813 and 2600, respectively. This demonstrates the material's crystal lattice is in a more strained state following UAM bonding, likely due to its increased dislocation density.

4. Discussion

The results presented here have demonstrated that significant changes occurred in materials following the UAM bonding process. To understand this, the microstructure evolution of the materials can be rationalized.

4.1. Microstructure evolution

As observed in the STEM images of the foil samples (Fig. 3 & Fig. 10), the materials before bonding have a large grain structure with tangled dislocations, likely from the rolling process to make the foils. The original O Foil microstructure has a dislocation cell structure ($\rho = 1.06 \times 10^{10} \text{ cm}^{-2}$) and a 0.00396 vol fraction of Mg_2Si precipitates, and the T4 Foil microstructure has dislocation tangles ($\rho = 1.68 \times 10^{10} \text{ cm}^{-2}$) with a 0.00148 vol fraction of Mg_2Si precipitates. After the UAM bonding process (Fig. 4 & Fig. 11), the bulk foil regions have relatively large grains (~600 nm) while the interfaces have extremely small grains (~100 nm). This suggests the UAM process caused significant plastic deformation to the interfaces during bonding, refining the grain structure. Despite the different starting microstructures between the two materials, the UAM plastic deformation refined the materials in a similar manner.

The STEM-EDS results (Fig. 5 & Fig. 12) suggest that the Mg_2Si precipitates are no longer present near the UAM interfaces. Instead, clusters of silicon are present, and the interface is enriched with

magnesium. This suggests the atoms within the precipitate debonded, and the magnesium atoms diffused towards the interface. For the Al 6061 alloy, the covalently bonded Mg_2Si precipitate has an equilibrium solubility limit of approximately 595 °C [70]. Therefore, below this solubility temperature, the magnesium and silica in the Al 6061 alloy should exist in a stable Mg_2Si precipitate phase within the aluminum matrix. If the aluminum alloy is brought above this temperature and rapidly cooled, such as in the heat affected zone of TIG welding, a solid solution of solute elements can be created [71,72]. If the material is not brought above this solubility limit, it is currently unknown how the precipitates could have dissolved. To the authors' knowledge, the only other known studies of Mg_2Si precipitates dissolving at low temperature are the result of an acidic corrosive environment for several hours [73, 74]. It is hypothesized that the plastic deformation from the UAM process resulted in the dissolution of the precipitates and/or could have decreased the solubility limit.

Once the elements debonded, there was elemental diffusion of the magnesium towards the interface. To rationalize the diffusion of magnesium, traditional diffusion expressions using Fick's Laws and Brownian motion can be considered. Previous UAM studies with embedded thermocouples and thermal imaging cameras have been used to estimate thermal profiles during UAM bonding [35,75–79]. Given the current UAM processing conditions, a peak temperature could be around 200 °C, although thermodynamic calculations of aluminum UAM bonding suggest temperatures could rise up to 300 °C [22]. The exact thermal profile here is difficult to determine due to the rapid nature of the UAM bonding process. Given these considerations, a peak temperature of 250 °C can be assumed here, and the total thermal profile time t , including heating up and cooling down, is 0.5 s. Assuming the thermal profile as noted, the lattice diffusivity D of magnesium in aluminum from the Sigli et al. [80] review article is $10^{-14} \text{ cm}^2/\text{s}$.

Assuming the clusters of silicon in Fig. 5 & Fig. 12 are previous Mg_2Si precipitates, the distance from a silicon cluster to the magnesium enriched interface could be considered as a diffusion distance x . The diffusion distance here is approximately 1 μm . Given the estimated total bonding time of 0.5 s, Fick's 2nd law, $x \sim \sqrt{Dt}$, can be used to find an approximate diffusivity of the magnesium ($2 \times 10^{-8} \text{ cm}^2/\text{s}$). The

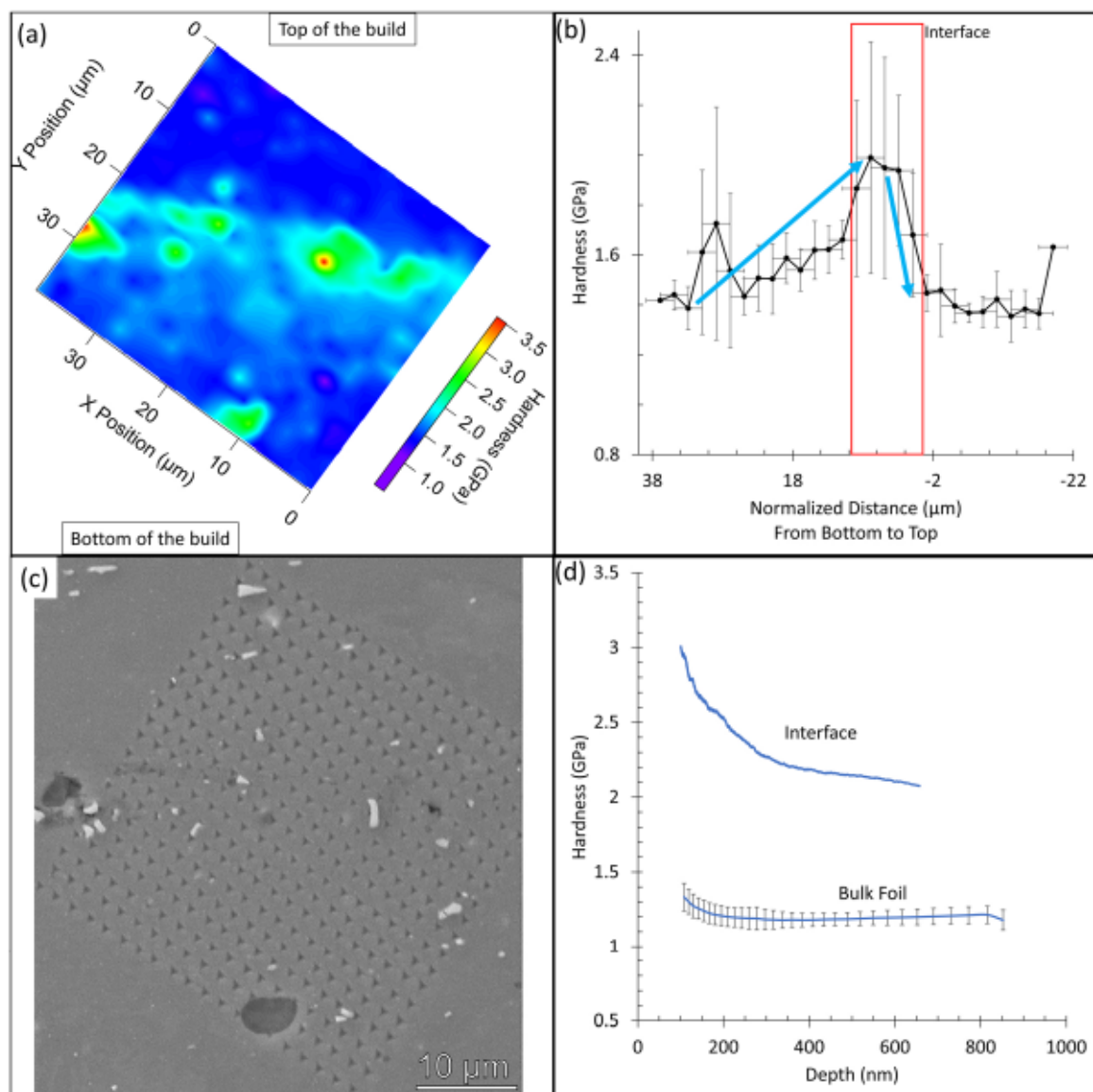


Fig. 14. Nanoindentation hardness map of the T4 UAM build. a) Hardness map, b) Average hardness line, c) SEM image of the indent array, d) Hardness vs depth for CSM indents.

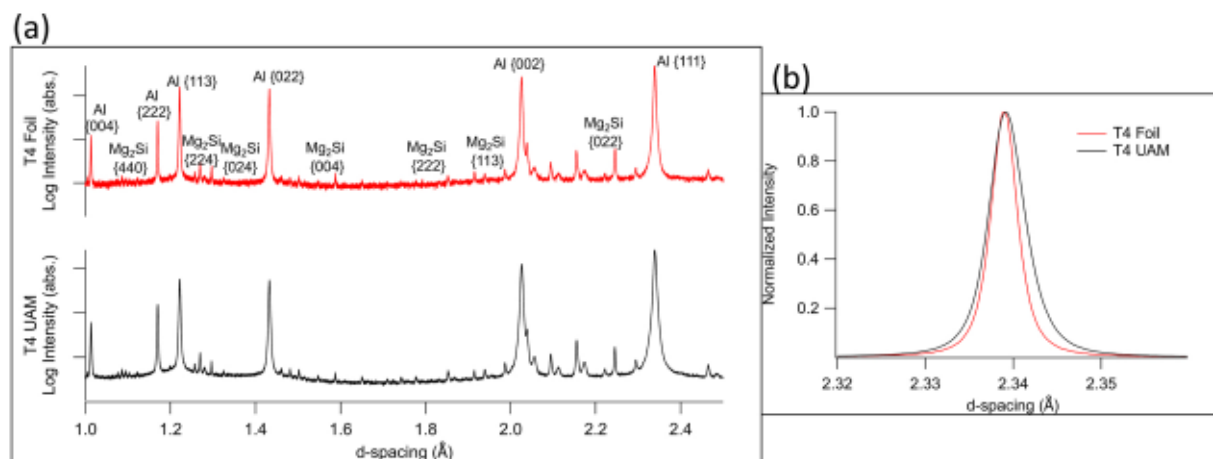


Fig. 15. XRD of the T4 Foil and T4 UAM samples. a) Diffraction patterns, b) Comparison of Al {111} peaks.

experimental diffusivity here is 6 orders of magnitude larger than the diffusivity predicted from the thermal profile. Clearly thermal diffusion cannot describe the observed atomic motion and additional diffusion processes are most likely present.

As Pagan et al. [8] suggested, accelerated diffusion could be possible at UAM interfaces from enhanced point defect vacancy concentrations caused by the severe plastic deformation. To calculate the enhanced vacancy concentration present, Brownian motion diffusion can be considered, as shown in Eq. 2. Here a_0 is the lattice constant, X_v is the vacancy concentration, ν is the Debye frequency of the atomic vibrations on its lattice site, E_m is the vacancy migration energy (0.61 eV in Al [81]), k is the Boltzmann constant (8.617×10^{-5} eV/K), and T is the absolute temperature [82–84].

$$D = a_0^2 X_v \nu \exp\left(-\frac{E_m}{kT}\right) \quad (2)$$

To rationalize the observed elemental diffusion, vacancy concentrations can be calculated at the UAM interface assuming the thermal profile, as noted above. These can be compared with the solubility limit temperature of the Mg_2Si precipitate and the thermal equilibrium concentration of vacancies (Table 2). This suggests a large concentration of vacancies was created from the plastic deformation associated with the UAM process. The plastic deformation and enhanced vacancy concentration could have also decreased the solubility limit of the Mg_2Si precipitate, resulting in the precipitate dissolving.

In addition to elevated vacancy concentrations, other short circuit diffusion pathways could also be present. The UAM process is known to cause dynamic recrystallization at the interfaces [1,17,20,28]. Recrystallization occurs as large plastic strains deform the crystals until they reorient into new lower energy crystals. The recrystallized grains are often separated by high angle grain boundaries (misorientation $> 15^\circ$) [57] which sweep across the material during the recrystallization event, sometimes more than once. Several UAM studies investigating grain boundary refinement have found a significant increase in the concentration of high angle grain boundaries at interfaces, and more high angle grain boundaries are observed during higher energy UAM [30,76]. In the present study, the high angle grain boundaries could provide additional diffusion pathways for the magnesium to travel. Finally, as noted in the X-ray diffraction results, high dislocation densities could be present in the samples. Pipe diffusion through dislocation cores could also occur during UAM bonding.

The effective diffusion through these other short circuit diffusion pathways can also be considered for comparison. The apparent diffusivity incorporating grain boundary diffusion is considered as:

$$D_{app} = D_l + \frac{\delta}{d} D_b \quad (3)$$

Here D_{app} is the apparent diffusivity, D_l is the lattice diffusivity, δ is the grain boundary width (0.5 nm), d is the grain size, and D_b is the grain boundary diffusivity. The total diffusivity is the diffusivity through the lattice summed with the grain boundary diffusivity as a fraction of available grain boundaries. Grain boundary diffusion in materials is a widely recognized phenomena but is poorly characterized for most metals. There are only a few experimental calculations of grain boundary diffusivity values. Therefore, estimates of the values in aluminum can only be considered here by referencing grain boundary diffusivity Arrhenius plots at various homologous temperatures in typical FCC metals [85,86]. A reported value of δD_b at the homologous temperature

Table 2

Vacancy concentrations created at the UAM interface compared with thermal equilibrium.

Temperature ($^\circ$ C)	X_v (Thermal equilibrium)	X_v (UAM interface)
250	6.0×10^{-7}	2.3×10^{-1}
595	1.6×10^{-4}	1.5×10^{-3}

of $0.43 T_m$ considered here is approximately 10^{-24} m³/s [87]. This value, along with the approximate interface grain size (~ 120 nm), can be used to estimate the apparent diffusivity including grain boundary diffusion. Here the diffusivity increases from 1×10^{-14} cm²/s to 8.4×10^{-14} cm²/s. Clearly there is roughly only one order of magnitude increase in diffusivity by considering grain boundary diffusion at the interface. The grain boundary diffusion considered high angle grain boundaries, which offer the largest orientation difference between grains and open space available for diffusing atoms. A tangled dislocation density represents a short circuit diffusion pathway that is less efficient than connected grain boundaries. Therefore, dislocation pipe diffusion would not raise the diffusivity above that grain boundary diffusion.

Following the enhanced diffusion, likely through elevated vacancy concentrations, other microstructure features along the O UAM and T4 UAM interfaces can be explored by STEM. There appear to be holes in the samples along grain boundaries and in the middle of grains directly at the interfaces. These could be artifacts due to TEM sample preparation using FIB, although they are only present at the interfaces. It is also possible these features could be vacancy clusters or voids related to the enhanced vacancy concentrations. The hypothesized UAM bonding temperature is 250° C. The onset temperature for vacancy migration (stage III recovery) has been thoroughly reviewed in most metals using isochronal annealing following particle irradiations, and the accepted value in aluminum is -73° C [62]. Above this temperature, mono-vacancies become mobile and can coalesce into vacancy clusters. Therefore, it is reasonable to assume that the enhanced concentration of mono-vacancies (which accelerated the magnesium diffusion) also resulted in monovacancies coalescing into visible vacancy clusters.

The next fundamental question is why there is preferential enhanced diffusion for magnesium atoms. This can be addressed by considering the free energy of the components in the UAM materials. An Ellingham diagram of the free energy of Mg_2Si , SiO_2 , Al_2O_3 , and MgO can quantify their likelihood of formation (Fig. 16). These free energies were calculated assuming a free gas environment, as opposed to precipitates inside an aluminum matrix. Therefore, the values only approximately represent formation of these species within a reasonable margin of error. In Ellingham diagrams, the standard reference state of an element is calculated as it reacts to form a potential compound (e.g., oxide, carbide, nitride, or intermetallic). The Gibbs free energy of formation for an element in its reference state is zero. Therefore, if an element has an affinity to form a compound, this will result in a decrease in the overall free energy of the system. When comparing multiple reactions, the component with the largest decrease in Gibbs free energy will be the most likely to form [88]. Considering the Ellingham diagram of the evaluated compounds, MgO has the greatest stability whereas Mg_2Si has

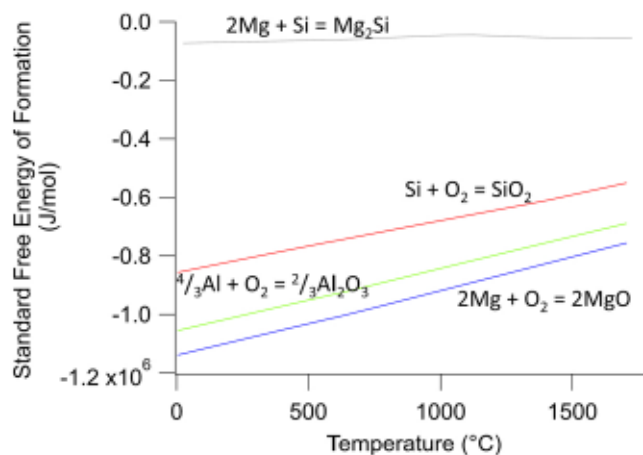


Fig. 16. Ellingham diagram of potential species in Al 6061 demonstrating MgO is most preferable to form.

the least. This suggests that once the magnesium separated from silicon, MgO could be preferentially formed. Although Ellingham diagrams do not provide guidance for reaction kinetics, the thermodynamic calculations demonstrate the feasibility of the magnesium and oxygen that are observed at the interface. Since the diffusivity of magnesium and silicon in an aluminum matrix are approximately equivalent [80], the kinetic process for preferable atomic movement of magnesium over silicon is currently unknown. The potential dissolution and diffusion of precipitate atoms during UAM should be considered by future researchers.

4.2. Evaluation of strengthening

The overall strength of the Al 6061 material is determined by several factors in the bulk foil regions and at the foil-foil interfaces. As noted from the EDS analysis, the Mg₂Si precipitates are present everywhere except the interfaces. Since these precipitates are several hundred nanometers in diameter, strengthening would occur as mobile dislocations bow around the precipitates, as opposed to shearing them. The classical approach for dislocation bowing strength [89] can be used.

$$\sigma = M \frac{Gb}{r} \sqrt{\frac{f}{V_f}} \quad (4)$$

Here M is the Taylor factor (~ 3.06 for equiaxed FCC and BCC materials), G is the shear modulus, b is the magnitude of the Burgers vector of the gliding dislocation, r is the radius of the precipitate, and V_f is the volume fraction of the precipitates in the matrix. Considering the observed size and spacing of the Mg₂Si precipitates, the dislocation bowing strengths would be approximately 27.8 MPa and 15.6 MPa in the *O UAM* bulk foil region and the *T4 UAM* bulk foil region, respectively.

Additionally, the materials contained a significant number of dislocations with densities of $1.06 \times 10^{10} \text{ cm}^{-2}$ in the *O Foil*, and $1.68 \times 10^{10} \text{ cm}^{-2}$ in the *T4 Foil*. Strain hardening can occur in materials as dislocation tangles interact with each other. This Frank-Read dislocation interaction can result in strain hardening and dislocation multiplication. The traditional equation for dislocation strain hardening [89] is:

$$\sigma = M \frac{Gb}{b} \sqrt{\rho} \quad (5)$$

M is the Taylor Factor, ρ is approximately 0.1, G is the shear modulus, b is the magnitude of the mobile dislocation Burgers vector, and ρ is the dislocation density. Using the dislocation density determined previously, the strain hardening prior to UAM bonding could be 23.4 MPa and 29.5 MPa for the *O UAM* and the *T4 UAM* bulk foil regions, respectively. These are approximately equivalent within experimental error. As noted from the X-ray diffraction data, the lattice strain increased after the UAM bonding, which could increase the strain hardening at the interfaces further. The utilization of the potential increase in strain hardening will be discussed further in the following section.

At the foil-foil interfaces, the grain sizes became significantly smaller. Hall [90] and Petch [91] described yield strength increase σ_{HP} from smaller grains d as a result from dislocations that pile up against grain boundaries. The specific material strength of a grain boundary to dislocations, k_y , has been thoroughly studied. As shown in the Cordero et al. review article, the commonly accepted k_y value for aluminum is $90 \text{ MPa} \cdot \text{m}^{1/2}$ [92]. This allows for the Hall-Petch equation to be used to rationalize the increased strength near the bonded interfaces from the reduced grain sizes, as determined earlier.

$$\sigma_{HP} = k_y d^{-1/2} \quad (6)$$

For the *O UAM* condition, the grain boundary strength at the interface would be 283 MPa, while the grain boundary strength in the bulk foil region would be 114 MPa. Therefore, the *O UAM* strength increase attributable to reduced grain sizes at the interface is 169 MPa. In a similar manner, the *T4 UAM* grain boundary strength at the interface is

254 MPa, while the grain boundary strength in the bulk foil region is 115 MPa. Therefore, the *T4 UAM* yield strength increase from reduced grain sizes at the interface is 139 MPa. The grain boundary strengthening at the interfaces of the *O UAM* sample and the *T4 UAM* sample increase by approximately a factor of two and are nearly equivalent within experimental error.

The vacancy clusters at the UAM interfaces could also contribute to strengthening. As migrating dislocations interact with vacancy clusters, they interact with the elastic strain field created by the clusters. The strain field from the empty lattice space is due to the volumetric dilation from the surrounding atoms. This strain field is proportional to the concentration of vacancy defects [31,93]. For large clusters acting as strong dislocation obstacles, the dispersed barrier Seeger model [31] can be used.

$$\sigma = M \frac{Gb}{b} \sqrt{\rho} \quad (7)$$

M is the Taylor factor, ρ is the defect cluster barrier strength which depends on the size of the voids (~ 1.0 for the present voids [94]), b is the shear modulus, b is the magnitude of the Burgers vector of the gliding dislocation, N is the cluster density, and d is the cluster diameter. Another potential model for describing the hardening from vacancy clusters is the weak barrier Friedel-Kroupa-Hirsch (FKH) model [95,96], in which the strength is proportional to $dN^{2/3}$. An estimate of the vacancy clusters size from the STEM images is $\sim 10 \text{ nm}$ for both the *O UAM* interface and the *T4 UAM* interface. The cluster density, within the radius of the low-depth indentation plastic zone field, is $\sim 9.1 \times 10^{14} \text{ cm}^{-3}$ for the *O UAM* interface and $2.3 \times 10^{14} \text{ cm}^{-3}$ for the *T4 UAM* interface. Using the Seeger strengthening model, this results in a predicted strength increase of 69 MPa for the *O UAM* interface and a strength increase of 34 MPa for the *T4 UAM* interface. Finally, it should be noted that the voids observed could have originated from vacancy clusters and been further expanded by TEM sample preparation. Therefore, the cluster sizes and strengths should be considered as upper limits rather than exact values. Additionally, it is possible that with large fractions of voids or cavities, mechanical softening can occur as opposed to hardening [97]. For voids well beyond 10 nanometers in size, softening has been attributed to the annihilation of dislocations as the large cavities act as dislocation sinks rather than dislocation obstacles [98].

Studies of UAM bonded Al 3003 H-18 [17] and Al 6061 H-18 [19] observed a decrease in bulk tensile strength, not an increase. To understand these differences, Sojiphan [20] hypothesized that UAM materials can be considered as a function of the overall stored energy. A cold rolled material (H-18 condition) has a higher initial energy state than an annealed material. This is due to the work hardening, grain deformation, and dislocation network created from cold rolling. If a cold rolled material is annealed, the stored energy will decrease as static recrystallization occurs. Alternatively, if a low energy annealed material is hot worked, the stored energy will increase due to the deformation process.

Sojiphan [20] further hypothesized that UAM structures are the result of the combination of dynamic recrystallization and dynamic recovery. A material will decrease in stored energy when static recrystallization dominates during bonding, while a material will increase in stored energy if dynamic recrystallization and dynamic recovery through adiabatic heating dominate during bonding. This causes recrystallization to occur slower, and the material ends up in a lower energy state [20]. A similar mechanism could be occurring in this present study. It is hypothesized that the tempered and annealed materials were in a low energy state prior to UAM bonding. After bonding, dynamic recrystallization occurred along with dynamic recovery and adiabatic heating. This hypothesis could also be connected to the microstructure features observed. The initial foils had intricate dislocation tangles and cell structures. After bonding, the foil bulk regions had relatively large grain structures without the dislocation cell wall structures. Additionally, the region with refined grain sizes is very small

(< 1 μm) compared to the width of other UAM interfaces with grain refinement (tens of μm) [7,10,16,22,28,77,99]. This could indicate that dynamic recrystallization was limited while dynamic recovery and adiabatic heating occurred. The annealed and tempered materials increased their energy state from the UAM bonding. This resulted in the observed microstructural changes and the increased tensile strength.

The nanoindentation data (Fig. 8 & Fig. 14) demonstrates the *O* UAM and *T4* UAM interfaces were harder than the bulk foil materials, although the indent depths were also different. Since there is a depth dependence to nanoindentation hardness, the indentation size effect must be considered. The indentation size effect refers to when shallow depth nanoindentation hardness values are larger than bulk hardness values as determined using traditional indentation techniques [100–106]. The Nix-Gao technique [107] is the most popular method to obtain estimates for bulk equivalent hardness from depth-dependent hardness data. Although it has received criticism [108–110], it is currently the best available method that can guide us. The Nix-Gao equation calculates the bulk equivalent hardness H_0 and the characteristic size effect length scale h^* using the hardness values H at their respective depths h [107].

$$\frac{H}{H_0} = \sqrt{1 + \frac{h^*}{h}} \quad (8)$$

When the hardness squared is plotted against the reciprocal of depth, the intercept of the line created is H_0^2 and the slope is related to h^* . The Nix-Gao hardness plots using the CSM indentation technique of the bulk foil region and the interface for the *O* UAM and *T4* UAM samples are shown in Fig. 17a. The bulk equivalent hardness of the *O* UAM sample in the bulk foil is 0.89 GPa with a h^* length parameter of 66.4 nm, while the interface has an equivalent hardness of 1.62 GPa and h^* of 279 nm. The bulk equivalent hardness of the *T4* UAM sample in the bulk foil is 1.16 GPa with h^* of 32.7 nm, and the interface has an equivalent hardness of 1.85 GPa with h^* of 549 nm. By comparing the bulk equivalent hardness for the bulk foil to the interface (Fig. 17b), clearly the interfaces are harder for both samples. Although the UAM interfaces have a hardness increase using depth dependent hardness measurements, the Nix-Gao approximation demonstrates that the interfaces have a very weak depth-dependent hardness increase. This observation can be used for more accurate determination of the interface strengthening characteristics.

The Tabor relationship $H \sim 3\sigma_y$ [111,112] is commonly used to compare the traditional Vickers hardness to yield strength. Zhu et al. [113] recently demonstrated the Tabor relationship does not consider indentation surface pileup effects and could overestimate the yield strength determined from nanoindentation. Therefore, a more advanced

model for comparing the Nix-Gao bulk equivalent hardness to nano-indentation yield strength is $\sigma_y^{NI} = 0.285H_0$. For the *O* UAM sample, the nanoindentation yield strength is 250 MPa in the bulk foil and 460 MPa at the interface. The *T4* UAM sample has a nanoindentation yield strength of 330 MPa in the bulk foil and 530 MPa at the interface.

4.3. Composite model of hardening

As described previously, the UAM process resulted in a complex microstructure evolution and an array of various dislocation obstacles. Tensile testing from the UAM build occurred with a load applied parallel to the foil-foil interface. This is a classic iso-strain condition (Voigt condition) as described by Courtney [114] and illustrated in Fig. 18. Since the tensile axis is parallel to the interface axis, the total stress exerted on the material σ_c is the sum of the forces experienced by each of the material sections (σ_{foil} and $\sigma_{\text{interface}}$) multiplied by their relative volume fraction (V_{foil} and $V_{\text{interface}}$) [114].

$$\sigma_c = \sigma_{\text{foil}}V_{\text{foil}} + \sigma_{\text{interface}}V_{\text{interface}} \quad (9)$$

As determined by the STEM-EDS analysis, the bulk foil region is strengthened by dislocation bowing and dislocation forest interactions. The STEM and XRD analysis demonstrate that the interfaces have dislocation obstacles of reduced grain sizes, vacancy clusters, and increased lattice strain, likely from elevated dislocation densities. Since these microstructure obstacles are considered long-range dislocation obstacles with comparable strengths, it is appropriate to combine them at each location using a root mean square superposition approach [89, 115,116]. The overall UAM build can be described as a composite structure using a combination of the microstructure features at the

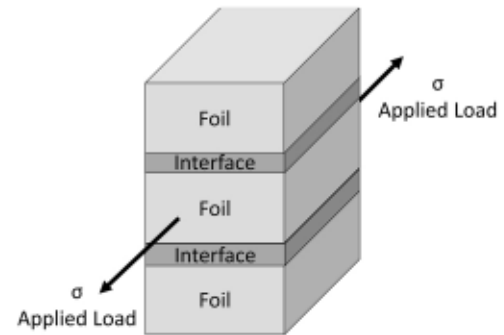


Fig. 18. Voigt iso-strain condition of the foils and interface.

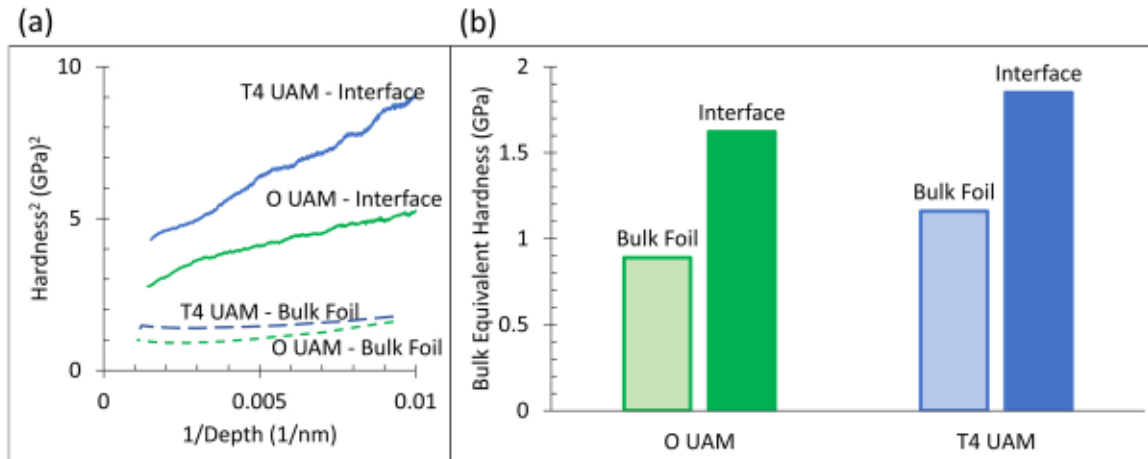


Fig. 17. Analysis of indentation hardness increase. a) Nix-Gao relationship for the *O* UAM and *T4* UAM conditions, b) Bulk equivalent hardness values in the bulk foil interior and at the interfaces.

various locations:

(10)

The strengthening contribution at the interface from grain boundaries is much larger than contributions from vacancy clusters or additional dislocation densities. Using the upper limit approximation of vacancy cluster strengthening, the contribution would be less than 8% of the composite strength. Although cluster strengthening values were calculated earlier, it should be repeated that these values represent liberal maximums since FIB damage could have exaggerated their size. Therefore, their potential contribution to the overall strengthening should be considered as near the maximum limit. In a similar manner, considering if the dislocation density at the interface reached as high as 10^{12} cm^{-2} (the maximum achievable limit), the contribution from Frank-Read type interactions could contribute less than 4% to the overall strengthening. Since these two dislocation obstacles provide negligible contributions to the strengthening, they can be safely ignored in this present analysis. Therefore, the composite strengthening equation can be considered as:

(11)

If an estimate of the volume fraction of the interfaces to the volume fraction of the foil were determined by the ratio of the width of the refined grains at the interfaces to the width of the bonded foils, the volume fraction of the foil would be 99% and the interfaces would be 1%. Using the previous calculations of strain hardening, dislocation bowing, and Hall-Petch strength, the σ_{UAM} is approximately 37.6 MPa for the *O* UAM sample and 34.4 MPa for the *T4* UAM sample. These calculations would signify that the interface has negligible contributions to the overall strength of the material. This is not the case, and it contradicts the previous experimental results. The interfaces became harder than the bulk material and they significantly increased the strength of the overall composite material. Instead, the Voigt model estimates the interfaces are only a small component of the composite strength.

The Voigt model also does not capture if the interface and foil regions enter plastic deformation at different applied displacements. As shown from the tensile testing results, the foils have a lower yield strength than the built structure. Therefore, if the built structure is a composite of the foil regions and the interfaces, it is likely that the foil regions reached their yield strength and began plastic deformation prior to the interfaces reaching their yield point. This is also supported by the differences in the bulk equivalent hardness values of the interfaces and bulk foil regions. During tensile testing, there is a simultaneous combination of elastic and plastic deformation in the interfaces and foil regions. This is a non-trivial consideration that the Voigt model cannot predict. This could have contributed to the strength differences found between the tensile testing and the composite model.

4.4. Experimental uncertainties and future considerations

Finally, the spatial location and errors of the analysis regions should be considered. During UAM bonding, the rolling and vibrating sonotrode induces a nonuniform distribution of plastic deformation. The distribution of induced plastic strain is due to several factors including the surface roughness of the sonotrode, the surface roughness of the bonding foil, and the spatial location and angle of each with respect to the other. These factors induce plastic deformation differences at various locations, which can then alter the observed microstructure. The refined microstructure features observed here were less than 0.5 μm in width. Variations in the microstructure could exist at different spatial locations, which low-resolution techniques like SEM cannot detect. A thorough high-resolution examination of all spatial locations in three dimensions could be a valuable study to capture the range of developed features,

although this is not practical within this scope of study.

Additionally, although UAM bonding is a shear deformation process, crystallographic texture changes were not considered here, like they have been elsewhere [6,20,27,30,117]. Texture analyses of UAM bonded aluminum have demonstrated that foil-foil interfaces can change from mostly an S3 texture to a rotated cube texture, while regions of material outside the interface are mostly unaffected [20]. Although texture development during bonding of pretreated aluminum could potentially differ from literature, the effect on mechanical strengthening would be secondary or tertiary. Strength differences due to crystallographic orientation are calculated through the Schmid factor. For each grain, the Schmid factor can range between 0 and 0.5 depending on the orientation of a grain's slip plane and direction with respect to the orientation of the applied stress [89]. The significant increase in observed tensile yield strength could only come if new dislocation obstacles were created at the interfaces. Individual crystal orientations, that provide only a small strength difference, would provide minimal strength changes. The small strength differences due to texture are comparable with the various experimental errors described in the text.

Bonding process parameters were also not categorically examined in this study. Settings were used to optimize the welding, while other studies have more carefully examined UAM process parameters [5,26,118–121]. The microstructures before and after bonding were provided to describe the observed effects. A full parameter window that creates the observed features has not yet been established. It is considered here that the pretreated materials increased their internal stored strain during the plastic deformation bonding. The plastic deformation resulted in lattice defect creation, atomic migration, and grain structure refinement. A potential process window for future researchers includes varying the magnitude of plastic deformation through changing the induced plastic strain rate, bonding temperature, or the material's internal strain energy.

5. Summary and conclusion

Microstructure evolution and strengthening effects from Ultrasonic Additive Manufacturing (UAM) were evaluated here. Al 6061 was pretreated into the annealed *O* and tempered *T4* conditions, then after UAM bonding, tensile testing (in the rolling x-direction) revealed the bonded material became significantly stronger. Nanoindentation characterization revealed that the foil-foil interfaces of the bonded materials became much stronger than the bulk foil regions. Significant crystal lattice changes occurred at the interface regions that resulted in the overall strengthening. This includes an increase in aluminum lattice strain, Mg_2Si precipitates dissolving, creation of point defect vacancies, enhanced diffusion of magnesium atoms, mono-vacancies coalescing into vacancy clusters, and refinement of grain sizes. These microstructure changes occurred from dynamic recrystallization, dynamic recovery, and adiabatic heating of the material.

CRedit authorship contribution statement

Jinschek Joerg R.: Writing review & editing, Supervision. **Babu S. S.:** Writing review & editing, Supervision, Funding acquisition. **Zinkle Steven J.:** Writing review & editing, Supervision. **Headings Leon M.:** Writing review & editing, Supervision. **Zhao Ningxin:** Writing review & editing, Formal analysis, Data curation. **Pagan Michael:** Writing review & editing, Writing original draft, Visualization, Methodology, Investigation, Formal analysis, Data curation. **Vijayan Sriram:** Writing review & editing, Investigation, Formal analysis, Data curation. **Dapino Marcelo J.:** Writing review & editing, Supervision, Funding acquisition.

Declaration of competing interest

The authors declare that they have no known competing financial interests or personal relationships that could have appeared to influence the work reported in this paper.

Data availability

Data will be made available on request.

Acknowledgements

Preconditioning of the aluminum was performed at the Center for Ultrasonic Additive Manufacturing located at The Ohio State University (OSU). The UAM bonding, tensile testing, and transmission electron microscopy (TEM) was also performed at OSU. Scanning electron microscopy (SEM) and TEM preparation using Focused Ion Beam (FIB) machining was performed at University of Tennessee, Knoxville (UTK) Institute for Advanced Materials and Manufacturing (IAMMM). Transmission Electron microscopy was performed at the Center for Electron Microscopy and Analysis (CEMAS) at The Ohio State University. Nano-indentation was performed in collaboration with Jennifer Hay at KLA-Tencor. Use of the Advanced Photon Source at Argonne National Laboratory was supported by the U. S. Department of Energy, Office of Science, Office of Basic Energy Sciences, under Contract No. DE-AC02-06CH11357. Funding for this research was supplied from the Air Force National Laboratory under contract FA864920P0998. Work at the Oak Ridge National Laboratory Manufacturing Demonstration Facility was supported by the DOE Office of Energy Efficiency And Renewable Energy (EERE) Advanced Manufacturing Offices (AMO). The OSU co-authors wish to acknowledge the financial support from the member organizations of the Smart Vehicle Concepts Center, a Phase III National Science Foundation Industry-University Cooperative Research Center (www.SmartVehicleCenter.org) under grant NSF IIP 1738723.

Appendix A. Supporting information

Supplementary data associated with this article can be found in the online version at [doi:10.1016/j.addma.2022.103228](https://doi.org/10.1016/j.addma.2022.103228).

References

- [1] N. Sridharan, C.M. Petrie, Ultrasonic additive manufacturing, *ASM Handb.* 24 (2020) 247–260, <https://doi.org/10.1201/9781315119106>.
- [2] K. Graff, Ultrasonic additive manufacturing, *ASM Handb.* 6A (2011) 731–741, <https://doi.org/10.31399/asm.hb.v06a.a0005605>.
- [3] J.O. Obielodan, B.E. Stucker, E. Martinez, J.L. Martinez, D.H. Hernandez, L.E. Murr D.a.ramirez, Optimization of the shear strengths of ultrasonically consolidated Ti/Al 3003 dual-material structures, *J. Mater. Process. Technol.* 211 (2011) 988–995, <https://doi.org/10.1016/j.jmatprotec.2010.12.017>.
- [4] P.J. Wolcott, N. Sridharan, S.S. Babu, A. Miriyev, N. Frage, M.J. Dapino, Characterisation of Al Ti dissimilar material joints fabricated using ultrasonic additive manufacturing, *Sci. Technol. Weld. Join.* 21 (2016) 114–123, <https://doi.org/10.1179/1362171815Y.0000000072>.
- [5] C.D. Hopkins, M.J. Dapino, S.A. Fernandez, Statistical characterization of ultrasonic additive manufacturing Ti/Al composites, *J. Eng. Mater. Technol. Trans.* 132 (2010) 1–9, <https://doi.org/10.1115/1.4002073>.
- [6] N. Sridharan, P. Wolcott, M. Dapino, S.S. Babu, Microstructure and texture evolution in aluminum and commercially pure titanium dissimilar welds fabricated using ultrasonic additive manufacturing, *Scr. Mater.* 117 (2016) 1–5, <https://doi.org/10.1016/j.scriptamat.2016.02.013>.
- [7] A.G. Truog, Bond Improvement of Al/Cu Joints Created by Very High Power Ultrasonic Additive Manufacturing (MS thesis), Ohio State University, 2012.
- [8] M. Pagan, C. Petrie, D. Leonard, N. Sridharan, S. Zinkle, S.S. Babu, Interdiffusion of elements during ultrasonic additive manufacturing, *Metall. Mater. Trans. A* 52 (2021) 1142–1157, <https://doi.org/10.1007/s11661-020-06131-2>.
- [9] C.-H. Kuo, N. Sridharan, T. Han, M.J. Dapino, S.S. Babu, Ultrasonic additive manufacturing of 4130 steel using Ni interlayers, *Sci. Technol. Weld. Join.* 24 (2019) 382–390, <https://doi.org/10.1080/13621718.2019.1607486>.
- [10] N. Sridharan, M. Norfolk, S.S. Babu, Characterization of Steel-Ta dissimilar metal builds made using very high power ultrasonic additive manufacturing (VHP-UAM), *Metall. Mater. Trans. A* 47 (2016) 2517–2528, <https://doi.org/10.1007/s11661-016-3354-5>.
- [11] C.M. Petrie, N. Sridharan, M. Subramanian, A. Hehr, M. Norfolk, J. Sheridan, Embedded metallized optical fibers for high temperature applications, *Smart Mater. Struct.* 28 (2019), 055012, <https://doi.org/10.1088/1361-665x/ab0b4e>.
- [12] R.J. Friel, R.A. Harris, Ultrasonic additive manufacturing - a hybrid production process for novel functional products, *Procedia CIRP* 6 (2013) 35–40, <https://doi.org/10.1016/j.procir.2013.03.004>.
- [13] P.J. Wolcott, M.J. Dapino, Ultrasonic additive manufacturing, *Addit. Manuf. Handb. Prod. Dev. Def. Ind.* (2017) 275–313, <https://doi.org/10.1201/9781315119106>.
- [14] C.M. Petrie, N. Sridharan, A. Hehr, M. Norfolk, J. Sheridan, High-temperature strain monitoring of stainless steel using fiber optics embedded in ultrasonically consolidated nickel layers, *Smart Mater. Struct.* 28 (2019), 085041, <https://doi.org/10.1088/1361-665x/ab2a27>.
- [15] M.J. Dapino, Smart structure integration through ultrasonic additive manufacturing, in: *Proceedings of the Conf. Smart Mater. Adapt. Struct. Intell. Syst. SMASIS 2014*, ASME 2014. 2 (2014) 1–8, doi: [10.1115/SMASIS20147710](https://doi.org/10.1115/SMASIS20147710).
- [16] D.E. Schick, Characterization of Aluminum 3003 Ultrasonic Additive Manufacturing (MS thesis), Ohio State University, 2009.
- [17] D.E. Schick, R.M. Hahnlen, R.R. Dehoff, P. Collins, S.S. Babu, M.J. Dapino, J. C. Lippold, Microstructural characterization of bonding interfaces in aluminum 3003 blocks fabricated by ultrasonic additive manufacturing, *Weld. J.* 89 (2010) 105–115.
- [18] T. Han, C.-H. Kuo, N. Sridharan, L.M. Headings, S.S. Babu, M.J. Dapino, Effect of preheat temperature and post-process treatment on the microstructure and mechanical properties of stainless steel 410 made via ultrasonic additive manufacturing, *Mater. Sci. Eng. A* 769 (2020), 138457, <https://doi.org/10.1016/j.msea.2019.138457>.
- [19] N. Sridharan, M. Gussev, R. Seibert, C.M. Parish, M. Norfolk, K. Terrani, S. S. Babu, Rationalization of anisotropic mechanical properties of Al-6061 fabricated using ultrasonic additive manufacturing, *Acta Mater.* 117 (2016) 228–237, <https://doi.org/10.1016/j.actamat.2016.06.048>.
- [20] K. Sojiphan, Effects of Very High Power Ultrasonic Additive Manufacturing Process Parameters on Hardness, Microstructure, and Texture of Aluminum 3003-H18 Alloy (Ph.D. dissertation), Ohio State University, 2015.
- [21] M.R. Sriraman, H.T. Fujii, M. Gonser, S.S. Babu, M. Short, Bond characterization in very high power ultrasonic additive manufacturing, in: *Proceedings of the Twenty First Annu. Int. Solid Free. Fabr. Symp. - An Addit. Manuf. Conf. SFF* 2010, (2010) 372–382.
- [22] M.R. Sriraman, S.S. Babu, M. Short, Bonding characteristics during very high power ultrasonic additive manufacturing of copper, *Scr. Mater.* 62 (2010) 560–563, <https://doi.org/10.1016/j.scriptamat.2009.12.040>.
- [23] D. Li, R.C. Soar, Plastic flow and work hardening of Al alloy matrices during ultrasonic consolidation fibre embedding process, *Mater. Sci. Eng. A* 498 (2008) 421–429, <https://doi.org/10.1016/j.msea.2008.08.037>.
- [24] M. Pagan, T. Ohmura, W. Ling, S.J. Zinkle, S.S. Babu, Strengthening effects at dissimilar metal interfaces created by ultrasonic additive manufacturing, *Metall. Mater. Trans. A* (2022) 3547–3564, <https://doi.org/10.1007/s11661-022-06776-1>.
- [25] A.W. Society, C3.2M/C3.2:2019 standard method for evaluating the strength of brazed joints, *Weld. Des. Fabr.* (2019) 12.
- [26] T. Han, L.M. Headings, R. Hahnlen, M.J. Dapino, Effect of process parameters on interfacial temperature and shear strength of ultrasonic additive manufacturing of carbon steel 4130, *J. Manuf. Sci. Eng.* 144 (2022) 1–7, <https://doi.org/10.1115/1.4053278>.
- [27] C.P. Massey, C.J. Havrilak, M.N. Gussev, K.A. Terrani, A.T. Nelson, Ultrasonic additive manufacturing of zirconium: pilot results, *Mater. Lett.* 302 (2021), 130330, <https://doi.org/10.1016/j.matlet.2021.130330>.
- [28] R.R. Dehoff, S.S. Babu, Characterization of interfacial microstructures in 3003 aluminum alloy blocks fabricated by ultrasonic additive manufacturing, *Acta Mater.* 58 (2010) 4305–4315, <https://doi.org/10.1016/j.actamat.2010.03.006>.
- [29] C. Zhang, L. Li, A coupled thermal-mechanical analysis of ultrasonic bonding mechanism, *Metall. Mater. Trans. B* 40 (2009) 196–207, <https://doi.org/10.1007/s11663-008-9224-9>.
- [30] H.T. Fujii, M.R. Sriraman, S.S. Babu, Quantitative evaluation of bulk and interface microstructures in Al-3003 alloy builds made by very high power ultrasonic additive manufacturing, *Metall. Mater. Trans. A* 42 (2011) 4045–4055, <https://doi.org/10.1007/s11661-011-0805-x>.
- [31] A. Seeger, Dispersed Barrier Modeling, in: *Proceedings of the Second UN Conf Peac. Uses At. Energy*, Geneva, 6, 1958, 250.
- [32] J. Friedel, *Dislocations*, 1st Englis, Pergamon Press, Oxford, 1964.
- [33] F. Seitz, On the generation of vacancies by moving dislocations, *Adv. Phys.* 8732 (1952) 43–90, <https://doi.org/10.1080/00018735200101161>.
- [34] D. Hull, D.J. Bacon, *Introduction to Dislocations*, fifth ed., Elsevier Ltd, 2011.
- [35] Y.C. Chen, D. Bakavos, A. Gholinia, P.B. Prangnell, HAZ development and accelerated post-weld natural ageing in ultrasonic spot welding aluminium 611-T4 automotive sheet, *Acta Mater.* 60 (2012) 2816–2828, <https://doi.org/10.1016/j.actamat.2012.01.047>.
- [36] ASM, *Heat Treating of Aluminum Alloys*, ASM Handb, 4, 1991, pp. 841–879, <https://doi.org/10.1361/asmhba000>.
- [37] C.M. Magazzeni, H.M. Gardner, I. Howe, P. Gopon, J.C. Waite, D. Rugg, D.E. J. Armstrong, A.J. Wilkinson, Nanoindentation in multi-modal map combinations: a correlative approach to local mechanical property assessment, *J. Mater. Res* 36 (2021) 2235–2250, <https://doi.org/10.1557/s43578-020-00035-y>.

- [38] W.C. Oliver, G.M. Pharr, An improved technique for determining hardness and elastic modulus using load and displacement sensing indentation experiments, *J. Mater. Res.* 7 (1992) 1564–1583, <https://doi.org/10.1557/JMR.1992.1564>.
- [39] X. Li, B. Bhushan, A review of nanoindentation continuous stiffness measurement technique and its applications, *Mater. Charact.* 48 (2001) 11–36, [https://doi.org/10.1016/S1044-5803\(02\)00192-4](https://doi.org/10.1016/S1044-5803(02)00192-4).
- [40] W.C. Oliver, G.M. Pharr, Measurement of hardness and elastic modulus by instrumented indentation: advances in understanding and refinements to methodology, *J. Mater. Res.* 19 (2004) 3–20, <https://doi.org/10.1557/jmr.2004.19.1.3>.
- [41] P.S. Phani, W.C. Oliver, A critical assessment of the effect of indentation spacing on the measurement of hardness and modulus using instrumented indentation testing, *Mater. Des.* 164 (2019), 107563, <https://doi.org/10.1016/j.matdes.2018.107563>.
- [42] Thermo-Calc Software, Thermo-Calc Software, (2021).
- [43] J.I. Goldstein, D.E. Newburg, P. Echlin, D.C. Joy, C. Fiori, E. Lifshin, Scanning electron, *Microsc. Microanal.* (1975), https://doi.org/10.1007/978-1-4684-2046-3_11.
- [44] A.N. Laboratory, Advanced Photon Source: Beamline 11-BM: High Resolution Powder Diffraction, U.S. Dep. Energy. (2018). <https://11bm.xray.aps.anl.gov/description.html>. (Accessed 3 May 2021).
- [45] G. Will, *Powder Diffraction: The Rietveld Method And The Two Stage Method To Determine and Refine Crystal Structures From Powder Diffraction Data*, Springer, 2006.
- [46] R.A. Young, *The Rietveld Method*, Oxford University Press, 1995.
- [47] G.F. Vander Voort, Practical applications of quantitative metallography, in: J. L. McCall, J.H. Steele (Eds.), *Pract. Appl. Quant. Metallogr.*, American Society for Testing and Materials, 1984, pp. 85–131, <https://doi.org/10.1520/stp36848s>.
- [48] R.K. Ham, The determination of dislocation densities in thin films, *Philos. Mag. A* 6 (1961) 1183–1184.
- [49] A. Considere, *Memoire Sur L'emploi Du Fer Et De L'acier Dans Les Constructions*, Ann. Ponts Chauss. 9 (1885) 574.
- [50] S. Kostic, J. Milojkovic, G. Simunovic, D. Vukelic, B. Tadic, Uncertainty in the determination of elastic modulus by tensile testing, *Eng. Sci. Technol. Int. J.* 25 (2022), 100998, <https://doi.org/10.1016/j.jestech.2021.05.002>.
- [51] J.D. Lord, R.M. Morrell, Elastic modulus measurement - obtaining reliable data from the tensile test, *Metrologia* 47 (2010) S14–S49, <https://doi.org/10.1088/0026-1394/47/2/S05>.
- [52] J.G. Kaufman, Understanding the aluminum temper designation system, *Introd. Alum. Alloy. Tempers* (2000) 39–76, <https://doi.org/10.1361/iaat2000p039>.
- [53] ASM International, *Wrought Aluminum (WA), Atlas Stress. Curves.* (2014) 299–309.
- [54] W.F. Smith, *Structure and Properties of Engineering Alloys*, 1981.
- [55] A.N. Abood, A.H. Saleh, Z.W. Abdullah, Effect of heat treatment on strain life of aluminum alloy AA 6061, *J. Mater. Sci. Res.* 2 (2013) 51–59, <https://doi.org/10.5539/jmsr.v2n2p51>.
- [56] J.G. Kaufman, Understanding wrought and cast aluminum alloys designations, *ASM Int. Chapter 3* (2000) 23–37, <https://doi.org/10.1361/iaat2000p023>.
- [57] K. Huang, R.E. Loge, A review of dynamic recrystallization phenomena in metallic materials, *Mater. Des.* 111 (2016) 548–574, <https://doi.org/10.1016/j.matdes.2016.09.012>.
- [58] J.G. Kaufman, *Introduction to Aluminum Alloys and Tempers*, ASM International, 2000.
- [59] J. Cizek, O. Melikhova, Z. Barnovska, I. Prochazka, R.K. Islamgaliev, Vacancy clusters in ultra fine grained metals prepared by severe plastic deformation, *J. Phys. Conf. Ser.* 443 (2013), <https://doi.org/10.1088/1742-6596/443/1/012008>.
- [60] N.Q. Vo, S. Odunuga, P. Bellon, R.S. Averback, Forced chemical mixing in immiscible alloys during severe plastic deformation at elevated temperatures, *Acta Mater.* 57 (2009) 3012–3019, <https://doi.org/10.1016/j.actamat.2009.03.007>.
- [61] S.J. Zinkle, B.N. Singh, Analysis of displacement damage and defect production under cascade damage conditions, *J. Nucl. Mater.* 199 (1993) 173–191, [https://doi.org/10.1016/0022-3115\(93\)90140-T](https://doi.org/10.1016/0022-3115(93)90140-T).
- [62] S.J. Zinkle, 1.03 - Radiation-induced effects on microstructure, *Compr. Nucl. Mater.* 1 (2012) 65–98, <https://doi.org/10.1016/B978-0-08-056033-5.00003-3>.
- [63] M. Kiritani, K. Urban, N. Yoshida, Formation of Submicroscopic vacancy clusters and radiation-induced refining in metals by electron-irradiation at high temperatures, *Radiat. Eff.* 61 (1982) 117–126, <https://doi.org/10.1080/00337578208225740>.
- [64] D.B. Williams, C.B. Carter, *Transmission Electron Microscopy*, Springer, 2011.
- [65] W.F. Gale, T.C. Totemeier, *Smithells Metals Reference Book*, Elsevier, 2004.
- [66] I. Guzman, E. Granda, J. Acevedo, A. Martínez, Y. Davila, R. Velazquez, Comparative in mechanical behavior of 6061 aluminum alloy welded by pulsed GMAW with different filler metals and heat treatments, *Materials* 12 (2019) 1–14, <https://doi.org/10.3390/ma1224157>.
- [67] A. Das, S.K. Das, S. Tarafder, Correlation of fractographic features with mechanical properties in systematically varied microstructures of Cu-strengthened high-strength low-alloy steel, *Metall. Mater. Trans. A* 40A (2009) 3138–3416, <https://doi.org/10.1007/s11661-009-9999-6>.
- [68] D. Broek, The role of inclusions and fracture, *Eng. Fract. Mech.* 5 (1972) 55–66.
- [69] B. Milkereit, L. Giersberg, O. Kessler, C. Schick, Isothermal time-temperature-precipitation diagram for an aluminum alloy 6005A in situ DSC experiments, *Materials* 7 (2014) 2631–2649, <https://doi.org/10.3390/ma7042631>.
- [70] Y. Tang, Y. Du, L. Zhang, X. Yuan, G. Kaptay, Thermodynamic description of the Al-Mg-Si system using a new formulation for the temperature dependence of the excess Gibbs energy, *Thermochim. Acta* 527 (2012) 131–142, <https://doi.org/10.1016/j.tca.2011.10.017>.
- [71] J. Qin, H. Nagaumi, C. Yu, F. Liu, Y. Li, L. Wang, Coarsening behavior of Mg2Si precipitates during post homogenization cooling process in Al-Mg-Si alloy, *J. Alloy. Compd.* 902 (2022), 162851, <https://doi.org/10.1016/j.jallcom.2021.162851>.
- [72] M. Hakem, S. Lebailli, S. Mathieu, D. Miroud, A. Lebailli, B. Cheniti, Effect of microstructure and precipitation phenomena on the mechanical behavior of AA6061-T6 aluminum alloy weld, *Int. J. Adv. Manuf. Technol.* 102 (2019) 2907–2918, <https://doi.org/10.1007/s00170-019-03401-1>.
- [73] E. Linardi, R. Haddad, L. Lanzani, Stability analysis of the Mg2Si phase in AA 6061 aluminum alloy, *Procedia Mater. Sci.* 1 (2012) 550–557, <https://doi.org/10.1016/j.mspro.2012.06.074>.
- [74] L.L. Li, B. Zhang, B. Tian, Y. Zhou, J.Q. Wang, E.H. Han, W. Ke, SVET study of Galvanic corrosion of Al/Mg 2 Si couple in aqueous solutions at different pH, *J. Electrochem. Soc.* 164 (2017) C240–C249, <https://doi.org/10.1149/2.0671706jes>.
- [75] M.R. Sriraman, M. Gonser, D. Foster, H.T. Fujii, S.S. Babu, M. Bloss, Thermal transients during processing of 3003 Al-H18 multilayer build by very high-power ultrasonic additive manufacturing, *Metall. Mater. Trans. B* 43B (2012) 133–144, <https://doi.org/10.1007/s11663-011-9590-6>.
- [76] M.R. Sriraman, M. Gonser, H.T. Fujii, S.S. Babu, M. Bloss, Thermal transients during processing of materials by very high power ultrasonic additive manufacturing, *J. Mater. Process. Technol.* 211 (2011) 1650–1657, <https://doi.org/10.1016/j.jmatprotec.2011.05.003>.
- [77] F. Haddadi, D. Tsivoulas, Grain structure, texture and mechanical property evolution of automotive aluminium sheet during high power ultrasonic welding, *Mater. Charact.* 118 (2016) 340–351, <https://doi.org/10.1016/j.matchar.2016.06.004>.
- [78] V.K. Patel, S.D. Bhole, D.L. Chen, Influence of ultrasonic spot welding on microstructure in a Magnesium A alloy, *Scr. Mater.* 65 (2011) 911–914, <https://doi.org/10.1016/j.scriptamat.2011.08.009>.
- [79] H.T. Fujii, Y. Goto, Y.S. Sato, H. Kokawa, Microstructure and lap shear strength of the weld interface in ultrasonic welding of Al alloy to stainless steel, *Scr. Mater.* 116 (2016) 135–138, <https://doi.org/10.1016/j.scriptamat.2016.02.004>.
- [80] C. Sigli, L. Maenner, C. Sztur, R. Shani, Phase diagram, solidification and heat treatment of aluminum alloys, *Alum. Alloy* 1 (1998) 87–98.
- [81] W.G. Wolfer, Fundamental properties of defects in metals, in: *Compr. Nucl. Mater.*, Elsevier Inc, 2012, pp. 1–45, <https://doi.org/10.1016/B978-0-08-056033-5.00001-X>.
- [82] R.W. Balluffi, S.M. Allen, W.C. Carter, *Kinetics of materials*, John Wiley & Sons, 2005.
- [83] A. Smigelskas, E. Kirkendall, Zinc diffusion in alpha brass, *Aime. XIII* (1946) 130, <https://doi.org/10.1103/PhysRevB.86.014426>.
- [84] P. Shewmon, Diffusion in Solid, *The Minerals, Metals & Materials Series*, Springer, 1979 <https://doi.org/10.1007/987-3-319-48206>.
- [85] R.W. Balluffi, M. Medalist, Grain boundary diffusion mechanisms in metals, *Inst. Met. Lect. 13* (1982) 527–553.
- [86] C. Herzog, S.V. Divinski, Grain boundary diffusion in metals: recent developments, *Mater. Trans.* 44 (2003) 14–27.
- [87] W. Gust, S. Mayer, A. Bogel, B. Predel, Generalized representation of grain boundary self-diffusion data, *J. Phys. Colloq.* 46 (1985). C4-537-C4-544.
- [88] H.J.T. Ellingham, Reducibility of oxides and sulphides in metallurgical processes, *J. Soc. Chem. Ind.* 53 (1944) 125–159, <https://doi.org/10.1002/jctb.5000534363>.
- [89] G.E. Dieter, *Mechanical Metallurgy*, third ed., McGraw-Hill, 2016.
- [90] E.O. Hall, The deformation and ageing of mild steel: III discussion of results, *Proc. Phys. Soc., Sec. B.* 64 (1951) 747–755.
- [91] N.J. Petch, The cleavage strength of polycrystals, *J. Iron Steel Inst.* 174 (1953) 25–28.
- [92] Z.C. Cordero, B.E. Knight, C.A. Schuh, Six decades of the Hall Petch effect – a survey of grain-size strengthening studies on pure metals, *Int. Mater. Rev.* 61 (2016) 495–512, <https://doi.org/10.1080/09506608.2016.1191808>.
- [93] Y.N. Osetsky, D.J. Bacon, Atomic-scale mechanisms of void hardening in bcc and fcc metals, *Philos. Mag.* 90 (2010) 945–961, <https://doi.org/10.1080/14786430903164580>.
- [94] L. Tan, J.T. Busby, Formulating the strength factor for improved predictability of radiation hardening, *J. Nucl. Mater.* 465 (2015) 724–730, <https://doi.org/10.1016/j.jnucmat.2015.07.009>.
- [95] J. Friedel, Weak Obstacle Model, in: *Dislocations*, Pergamon, New York, n.d.
- [96] F. Kroupa, P.B. Hirsch, Elastic interaction between prismatic dislocation loops and straight dislocations, *Discuss. Faraday Soc.* 38 (1964) 49–55, <https://doi.org/10.1039/DF9643800049>.
- [97] M.J. Worswick, R.J. Pick, Void growth and constitutive softening in a periodically voided solid, *J. Mech. Phys. Solids* 38 (1990) 601–625, [https://doi.org/10.1016/0022-5096\(90\)90025-Y](https://doi.org/10.1016/0022-5096(90)90025-Y).
- [98] L.X. Yang, S.J. Zheng, Y.T. Zhou, J. Zhang, Y.Q. Wang, C.B. Jiang, N.A. Mara, I. J. Beyerlein, X.L. Ma, Effects of He radiation on cavity distribution and hardness of bulk nanolayered Cu-Nb composites, *J. Nucl. Mater.* 487 (2017) 311–316, <https://doi.org/10.1016/j.jnucmat.2017.02.022>.
- [99] H.T. Fujii, S. Shimizu, Y.S. Sato, H. Kokawa, High-strain-rate deformation in ultrasonic additive manufacturing, *Scr. Mater.* 135 (2017) 125–129, <https://doi.org/10.1016/j.scriptamat.2016.12.030>.
- [100] N.A. Stelmashenko, M.G. Walls, L.M. Brown, Y.V. Milman, Microindentations on W and Mo oriented single crystals: an STM study, *Acta Metall. Mater.* 41 (1993) 2855–2865.

- [101] M.S. De Guzman, G. Neubauer, P. Flinn, W.D. Nix, The role of indentation depth on the measured hardness of materials, *Mater. Res. Soc. Proc.* 308 (1993) 613.
- [102] M. Atkinson, Further analysis of the size effect in indentation hardness test of some metals, *J. Mater. Res.* 10 (1995) 2908.
- [103] Q. Ma, D.R. Clarke, Size dependent hardness of silver single crystals, *J. Mater. Res.* 10 (1995) 853.
- [104] W.J. Poole, M.F. Ashby, N.A. Fleck, Micro-hardness of annealed and work-hardened copper polycrystals, *Scr. Mater.* 34 (1996) 559–564.
- [105] K.W. McElhaney, J.J. Vlassak, W.D. Nix, Determination of indenter tip geometry and indentation contact area for depth-sensing indentation experiments, *J. Mater. Res.* 13 (1998) 1300–1306, <https://doi.org/10.1557/JMR.1998.0185>.
- [106] S. Suresh, T.G. Nieh, B.W. Choi, Nano-indentation of copper thin films of silicon substrates, *Scr. Mater.* 41 (1999) 951–957.
- [107] W.D. Nix, H. Gao, Indentation size effects in crystalline materials: a law for strain gradient plasticity, *J. Mech. Phys. Solids* 46 (1998) 411–425, [https://doi.org/10.1016/S0022-5096\(97\)00086-0](https://doi.org/10.1016/S0022-5096(97)00086-0).
- [108] Y. Huang, F. Zhang, K.C. Hwang, W.D. Nix, G.M. Pharr, G. Feng, A model of size effects in nano-indentation, *J. Mech. Phys. Solids* 54 (2006) 1668–1686, <https://doi.org/10.1016/j.jmps.2006.02.002>.
- [109] Z. Wang, J. Zhang, A. Ma, A. Hartmaier, Y. Yan, T. Sun, On the crystallographic anisotropy of plastic zone size in single crystalline copper under Berkovich nanoindentation, *Mater. Today Commun.* 25 (2020), 101314, <https://doi.org/10.1016/j.mtcomm.2020.101314>.
- [110] G.M. Pharr, E.G. Herbert, Y. Gao, The indentation size effect: a critical examination of experimental observations and mechanistic interpretations, *Annu. Rev. Mater. Res.* 40 (2010) 271–292, <https://doi.org/10.1146/annurev-matsci-070909-104456>.
- [111] D. Tabor, The hardness of solids, *Rev. Phys. Technol.* 1 (1970) 145–179.
- [112] D. Tabor, Indentation hardness and its measurement: some cautionary comments, *microindentation*, *Tech. Mater. Sci. Eng.* 889 (1986) 129–159.
- [113] P. Zhu, Y. Zhao, S. Agarwal, J. Henry, S.J. Zinkle, Toward accurate evaluation of bulk hardness from nanoindentation testing at low indent depths, *Mater. Des.* 213 (2022), 110317, <https://doi.org/10.1016/j.matdes.2021.110317>.
- [114] T.H. Courtney, *Mechanical Behavior of Materials*, second ed., McGraw-Hill, 1990.
- [115] A.J.E. Foreman, M.J. Makin, Dislocation movement through random arrays of obstacles, *Philos. Mag. A* 14 (1966) 911–924.
- [116] G.R. Odette, G.E. Lucas, Recent progress in understanding reactor pressure vessel steel embrittlement, *Rad. Eff. Def. Solids* 144 (1998) 189–231, <https://doi.org/10.1080/10420159808229676>.
- [117] N. Sridharan, P. Wolcott, M. Dapino, S.S. Babu, Microstructure and mechanical property characterisation of aluminium steel joints fabricated using ultrasonic additive manufacturing, *Sci. Technol. Weld. Join.* 22 (2016) 373–380, <https://doi.org/10.1080/13621718.2016.1249644>.
- [118] P.J. Wolcott, A. Hehr, M.J. Dapino, Optimized welding parameters for Al 6061 ultrasonic additive manufactured structures, *J. Mater. Res.* 29 (2014) 2055–2065, <https://doi.org/10.1557/jmr.2014.139>.
- [119] C.Y. Kong, R.C. Soar, P.M. Dickens, Characterisation of aluminium alloy 6061 for the ultrasonic consolidation process, *Mater. Sci. Eng. A* 36A3 (2003) 99–106, [https://doi.org/10.1016/S0921-5093\(03\)00590-2](https://doi.org/10.1016/S0921-5093(03)00590-2).
- [120] C.Y. Kong, R.C. Soar, P.M. Dickens, Optimum process parameters for ultrasonic consolidation of 3003 aluminium, *J. Mater. Process. Technol.* 146 (2004) 181–187, <https://doi.org/10.1016/j.jmatprotec.2003.10.016>.
- [121] G.D.J. Ram, Y. Yang, B.E. Stucker, A. Engineering, Effect of process parameters on bond formation during ultrasonic consolidation of aluminum alloy 3003, *J. Manuf. Syst.* 25 (2006) 221–238, [https://doi.org/10.1016/S0278-6125\(07\)80011-2](https://doi.org/10.1016/S0278-6125(07)80011-2).